

Detection of the Yarkovsky effect for C-type asteroids in the Veritas family

V. Carruba^{1,3*}, D. Vokrouhlický², D. Nesvorný³

¹UNESP, Univ. Estadual Paulista, Grupo de dinâmica Orbital e Planetologia, Guaratinguetá, SP, 12516-410, Brazil

²Institute of Astronomy, Charles University, V Holešovičkách 2, Prague 8, CZ-18000, Czech Republic

³Department of Space Studies, Southwest Research Institute, Boulder, CO, 80302, USA

Accepted 2017 May 11. Received 2017 May 11; in original form 2017 March 2.

ABSTRACT

The age of a young asteroid family can be determined by tracking the orbits of family members backward in time and showing that they converge at some time in the past. Here we consider the Veritas family. We find that the membership of the Veritas family increased enormously since the last detailed analysis of the family. Using backward integration, we confirm the convergence of nodal longitudes Ω , and, for the first time, also obtain a simultaneous convergence of pericenter longitudes ϖ . The Veritas family is found to be $8.23_{-0.31}^{+0.37}$ Myr old. To obtain a tight convergence of Ω and ϖ , as expected from low ejection speeds of fragments, the Yarkovsky effect needs to be included in the modeling of the past orbital histories of Veritas family members. Using this method, we compute the Yarkovsky semi-major axis drift rates, da/dt , for 274 member asteroids. The distribution of da/dt values is consistent with a population of C-type objects with low densities and low thermal conductivities. The accuracy of individual da/dt measurements is limited by the effect of close encounters of member asteroids to (1) Ceres and other massive asteroids, which cannot be evaluated with confidence.

Key words: Minor planets, asteroids: general – celestial mechanics.

1 INTRODUCTION

Asteroid families are the outcomes of disruptive collisions of main belt asteroids. After a family-forming event, the orbits of fragments are affected by gravitational and non-gravitational forces, such as planetary perturbations and the Yarkovsky effect (Bottke et al. 2002; Vokrouhlický et al. 2015). The Yarkovsky effect acts to spread fragments in semi-major axis. It is therefore generally difficult, in case of old asteroid families, to distinguish between the original spread caused by ejection velocities and the subsequent evolution by the Yarkovsky effect.

For young asteroid families (ages <20 Myr), on the other hand, the semi-major axis spread is not affected by the Yarkovsky effect. Their orbital structure thus allows us to make inferences about the original ejection velocity field. This is why the young asteroid families are useful. In addition, by integrating the orbits of young family members backward in time and checking on the convergence of their longitudes of pericenter ϖ and node Ω , it is possible to determine the family’s age (Nesvorný et al. 2003).

The Veritas family (Family Identification Number,

FIN, 609; Nesvorný et al. (2015)) was first studied by Milani & Farinella (1994). They found that the orbit of (490) Veritas diffuses chaotically in eccentricity due to a background mean motion resonance. For (490) Veritas to be classified as a member, the family must be young (<50 Myr, Milani & Farinella (1994)). Subsequently, Nesvorný et al. (2003) used the convergence of Ω of Veritas members to determine that the family is only 8.3 Myr old. This very young age was linked to a spike in the terrestrial deposition of interplanetary dust particles at 8.2 ± 0.1 Myr ago (Farley et al. 2006).

Many asteroids have been discovered since 2003, and the population of Veritas members is now about ten times larger than it was back then. Using techniques developed in Carruba et al. (2016), here we investigate the interesting case of the Veritas family. Our goal is to: (i) revise the age estimate obtained in Nesvorný et al. (2003), (ii) show that the convergence constraint requires inclusion of the Yarkovsky effect in the backward integration, (iii) set constraints on values of the key parameters affecting the Yarkovsky force, such as the asteroids density and thermal conductivity, and (iv) study the effect close encounters with Ceres and other massive asteroids have had on the past orbital histories of family members.

* E-mail: vcarruba@feg.unesp.br

The analysis of the Veritas family is complicated by the presence of the nearby 2:1 resonance with Jupiter, where the precession rate of the perihelion longitude, g , has a singularity. The precession rate g is therefore fast in the region of the Veritas family, which prevented Nesvorný et al. (2003) from demonstrating the convergence of ϖ . Here we were able to overcome this difficulty and obtain, for the first time, the simultaneous convergence of both Ω and ϖ . This increases our confidence that the present analysis correctly estimates the age of the Veritas family and constrains the principal parameters of the Yarkovsky effect.

2 FAMILY IDENTIFICATION AND DYNAMICAL PROPERTIES

As a first step of our analysis, we obtained the membership of the Veritas family from Nesvorný et al. (2015), where the family was defined using the Hierarchical Clustering Method (HCM, (Bendjoya & Zappalà 2002)) and a cutoff of 30 m/s. 1294 members of the Veritas family were identified in that work. Following Carruba & Nesvorný (2016) we identified objects in the local background of the Veritas family. For this, we used the database of synthetic proper elements available at the AstDyS site (<http://hamilton.dm.unipi.it/astdys>, Knežević and Milani (2003)), accessed on September 3, 2016). Asteroids were considered to belong to the local background if they had proper e and $\sin i$ near the Veritas family, namely $0.035 < e < 0.095$ and $0.135 < \sin i < 0.185$ (these ranges correspond to four standard deviations of the observed distribution of the Veritas family).

The values of proper a were chosen from the maximum and minimum values of Veritas members plus or minus 0.02 au, the averaged expected orbital mobility potentially caused by close encounters with massive asteroids over 4 Gyr (Carruba et al. 2013). Namely, this corresponds to an interval $3.15 < a < 3.19$ au. Overall, we found 2166 background asteroids. No other important dynamical groups can be found in the local background of the Veritas family (Carruba 2013). After removing members of the Veritas family, the local background consists of 872 asteroids. The Veritas family and its background are shown in Fig. 1.

Chaotic dynamics in the region of the Veritas family was studied in detail in Milani & Farinella (1994) and Tsiganis et al. (2007). Interested readers can find more information in those papers. Here we just consider the information about Veritas family members that can be obtained from their Lyapunov times. Tsiganis et al. (2007) identified two main chaotic regions in the Veritas family: one, with Lyapunov times $< 3 \times 10^4$ yr, associated with the three-body resonance 5-2-2 (or 5J:-2S:-2A in alternative notation) and its multiplet structure, and another one, with $3 \times 10^4 < T_L < 10^5$ yr, caused by the interaction of asteroids with the 3+3-2 resonance (or 3J:3S:-2A). Another three-body resonance identified in the region was the 7-7-2 resonance, but that only affected a single asteroid ((37005) 2000 TO37).

Objects with Lyapunov times longer than 10^5 yr and semi-major axes lower than that of the 3+3-2 resonance were classified as R_1 objects, while regular asteroids between the 3+3-2 and 5-2-2 resonances were classified as R_2 asteroids

(Tsiganis et al. 2007). Only one regular Veritas family member was known with semi-major axis larger than that of the 5-2-2 resonance. A significant population of objects in this region is, however, currently known (139 asteroids, Fig. 1). Extending the notation from Tsiganis et al. (2007), we define these asteroids as being R_3 objects.

Concerning secular resonances in the region of the Veritas family, an extensive study of the secular dynamics was performed in Carruba (2013); Carruba et al. (2014). The two main secular resonances near the Veritas family are the $g - 2g_6 + g_5 + s - s_7$ (or, in terms of the linear secular resonances arguments, $2\nu_6 - \nu_5 + \nu_{17}$) and $g - g_6 + 2s - 2s_6$ (or $\nu_6 + 2\nu_{16}$) resonances. Only 10 outer main belt asteroids were found to librate in these resonances. They do not thus play a significant role in the dynamical evolution of the Veritas family.

Fig. 2 shows the (a, e) projection of asteroids near the Veritas family. The color code identifies the degree of chaoticity associated with a given orbit: regular orbits are shown as black dots, orbits with $3 \times 10^4 < T_L < 10^5$ yr are shown as green full circles, and orbits with $T_L < 3 \times 10^4$ yr are shown as blue full circles. With the exception of the new population of regular objects beyond the 5-2-2 resonance, our analysis essentially confirms that of Tsiganis et al. (2007).

3 PHYSICAL PROPERTIES

A detailed analysis of physical properties of asteroids in the region of the Themis, Hygiea and Veritas families was reported in Carruba (2013). Here we briefly summarize the physical properties of asteroids near the Veritas family. There are 146 objects with photometric data in the Sloan Digital Sky Survey-Moving Object Catalog data (SDSS-MOC4; Ivezić et al. (2001)) in this region, 89 of which (61% of the total) are members of the Veritas family. In addition, 784 objects have geometric albedo and absolute magnitude information available in the WISE and NEOWISE databases (Masiero et al. 2012).

Fig. 3 shows the taxonomic classification of asteroids obtained from SDSS-MOC4 with the method of DeMeo & Carry (2013) (panel A), and the WISE geometric albedo p_V (panel B). In panel B, we separate dark asteroids (compatible with the C-complex taxonomy; $p_V < 0.12$) and bright asteroids (S-complex taxonomy; $0.12 < p_V < 0.30$) (Masiero et al. 2012). The Veritas family is obviously a C-type family, and the C-complex objects also dominate the local background. In total, we found 97 Cs, 39 Xs and 3 Ds in the region, all belonging to the C complex. There were only 7 S-complex asteroids, 4 of which are S-type, 2 K-type, and 1 A-type. The proportion of C- and S-complex asteroids is consistent with the available geometric albedo data: of the 784 objects with WISE albedo, 715 (91.2% of the total) have $p_V < 0.12$, and are compatible with a C-complex taxonomy.

Finally, we estimated the masses of asteroids in and near the Veritas family assuming objects to be spherical with bulk density equal to 1300 kg m^{-3} (typical value of C-type objects). For objects with available WISE albedo data, we used the WISE p_V value to estimate their radius from the absolute magnitude (Eq. 1 in Carruba et al. (2003)). For all

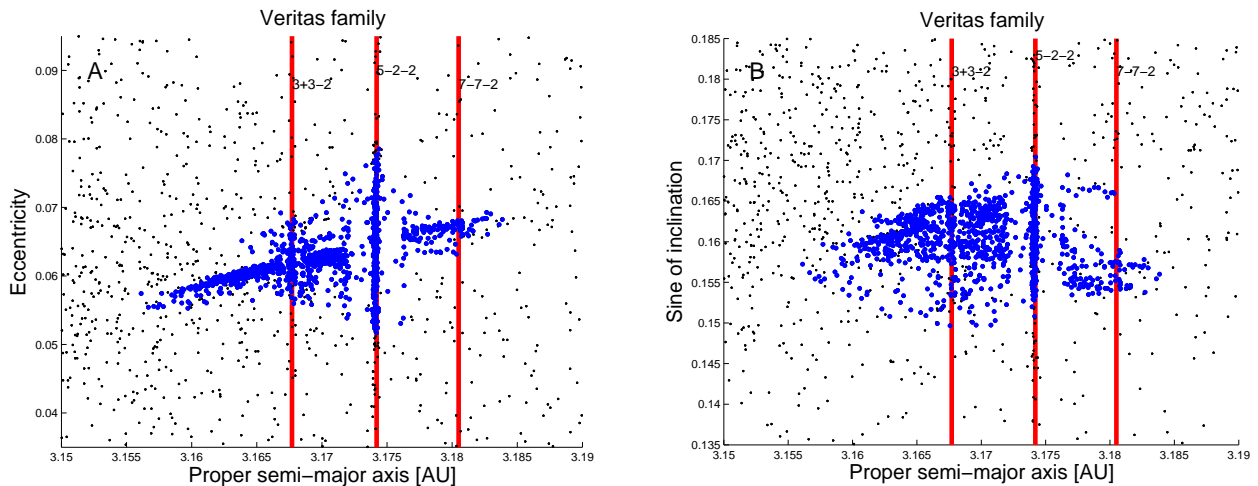


Figure 1. The (a, e) (panel A) and $(a, \sin i)$ (panel B) projections of orbits near the Veritas family. The vertical lines display the locations of main mean-motion resonances in the region. The blue symbols show the orbits of members of the Veritas family. The black dots display the background orbits.

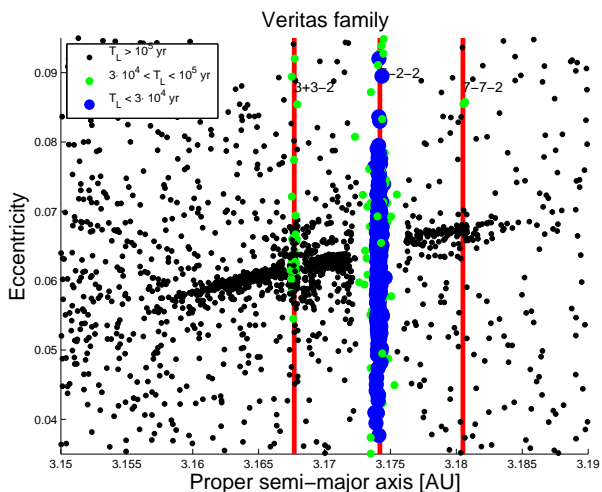


Figure 2. The (a, e) projection of orbits in the local background of the Veritas family. Objects with Lyapunov times $T_L > 10^5$ yr are shown as black dots, objects with $3 \times 10^4 < T_L < 10^5$ yr are displayed as green full circles, and objects with $T_L < 3 \times 10^4$ yr are shown as blue full circles. The Lyapunov times were obtained from the AstDyS catalog (Knežević and Milani (2003)).

other objects we used $p_V = 0.07$, which is the mean value of the Veritas family.

Fig. 4 shows our results. Among the Veritas members, only (490) Veritas and (1086) Nata have estimated masses larger than 10^{17} kg and diameters $D > 50$ km ($D = 110$ km and $D = 70$ km, respectively). SPH simulation of the catastrophic disruption event that produced the Veritas family (Michel et al. 2011) indicate the observed size distribution of family members cannot be well reproduced if both (490) Veritas and (1086) Nata are true members of the family. Our analysis of the past convergence described in the following sections shows that the convergence of (1086) Nata can be demonstrated, while that of (490) Veritas cannot (because of the chaotic orbit of (490) Veritas). While it is not possible at this stage to positively decide whether (490) Veritas

is a member or not of its namesake family, for the purpose of our research we will use the orbit of (1086) Nata as a reference for the method of convergence of secular angles hereafter. Finally, since the combined volume of the Veritas members, barring (490) Veritas itself, is about 40% of the total volume of the family, the family-forming event should be characterized as a catastrophic disruption.

4 PAST CONVERGENCE OF THE NODAL LONGITUDES

Following the approach described in Nesvorný et al. (2003); Nesvorný & Bottke (2004); Carruba et al. (2016) for the Veritas and Karin families, we checked for a past convergence of orbits of members of the Veritas family and objects in the local background. We first focus on demonstrating the convergence in Ω , because the convergence of ϖ is complicated by the proximity to the 2:1 resonance (both the g frequency and its derivative, $\partial g/\partial a$, are large) (Nesvorný et al. 2003).

To start with, to avoid strongly chaotic orbits, we selected 918 members of the Veritas dynamical family with $T_L > 3 \times 10^4$ yr. The chaotic orbits are mostly found in the identified three body resonances and we cannot use them because their orbital histories cannot be computed deterministically. The selected orbits were integrated backward in time with *SWIFT_MVSF*, which is a symplectic integrator programmed by Levison & Duncan (1994). It was modified by Brož (1999) to include online filtering of the osculating elements. All eight planets were included in the integration as massive perturbers. We used a time step of 1 day. The Yarkovsky effect was not included in this initial integration.

Using the approach described in Carruba et al. (2016), we first checked for the past convergence of Ω . Asteroid (1086) Nata was used as a reference body, because its orbit has very long Lyapunov time ((490) Veritas cannot be used for this purpose because its orbit in the 5-2-2 resonance is strongly chaotic). Specifically, we required that Ω of individual orbits converge to within $\pm 60^\circ$ about Nata's Ω

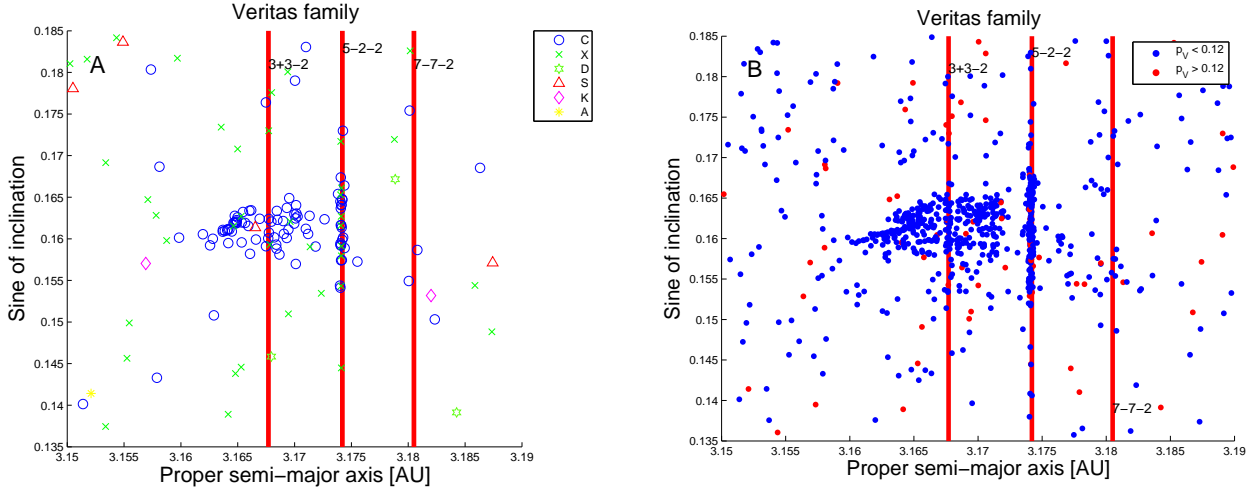


Figure 3. An $(a, \sin i)$ distribution of Veritas family asteroids, with taxonomic information (panel A) and WISE albedo data (panel B). Symbols used to identify asteroids with different spectral types and albedo values are identified in the inset.

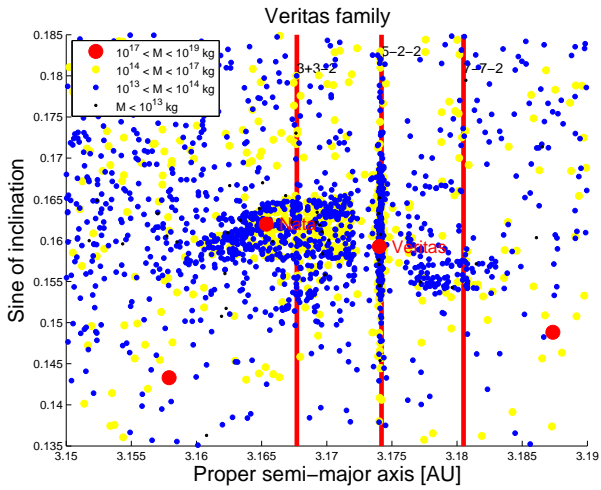


Figure 4. An $(a, \sin i)$ projection of asteroids near the orbital location of the Veritas family. The color and size of the symbols reflect the estimated asteroid mass.

in the time interval between 8.1 and 8.5 Myr ago, which encompasses the age of the Veritas family estimated in Nesvorný et al. (2003). Out of the 918 considered bodies, 705 (76.8% of the total) passed this test.

We then turned our attention to objects in the Veritas family background. First, as in Carruba et al. (2016), we computed the terminal ejection velocities for the 705 bodies that passed the above criterion by inverting Gauss equations (Murray & Dermott 1999):

$$\frac{\delta a}{a} = \frac{2}{na(1-e^2)^{1/2}} [(1+e \cos f)\delta v_t + e \sin f \delta v_r], \quad (1)$$

$$\delta e = \frac{(1-e^2)^{1/2}}{na} \left[\frac{e+2 \cos f + e \cos^2 f}{1+e \cos f} \delta v_t + \sin f \delta v_r \right], \quad (2)$$

$$\delta i = \frac{(1-e^2)^{1/2} \cos(\omega+f)}{na} \delta v_W. \quad (3)$$

where $\delta a = a - a_{ref}$, $\delta e = e - e_{ref}$, $\delta i = i - i_{ref}$, $a_{ref}, e_{ref}, i_{ref}$ define a reference orbit (we set $a_{ref} = 3.170$ au, $e_{ref} = 0.062$ and $i_{ref} = 9.207^\circ$) and f and ω are the true anomaly and perihelion argument of the disrupted body at the time of impact. As in Tsiganis et al. (2007), we used $f = 30^\circ$ and $\omega + f = 180^\circ$.

The highest terminal ejection velocities observed inferred from this exercise, excluding objects that obviously drifted away in the three-body resonances, was 200 m/s. We then integrated backward in time asteroids in the local background of the Veritas family as defined in Sect. 2 and eliminated objects that: (i) had Lyapunov times shorter than 3×10^4 yr, (ii) had ejection velocities with respect to the reference orbit larger than 220 m/s (i.e., 10% larger than the maximum value determined above), and (iii) did not show the convergence of Ω to within $\pm 60^\circ$ around that of (1086) Nata between 8.1 and 8.5 Myr ago.

Only 31 asteroids satisfied these requirements. Since, however, most of these objects were located at semi-major axis significantly smaller than those of the HCM members of the Veritas family (Fig. 5, panel A), we decided not to consider them for the following analysis. After eliminating taxonomical interlopers, we were left with 704 members of the Veritas family. Fig. 5, panel A, shows the orbits of 704 members. Panel B of that figure illustrates the convergence of nodal longitudes at $\simeq 8.3$ Myr ago.

5 FAMILY AGE AND DETECTION OF THE YARKOVSKY EFFECT

The next step of our analysis is to obtain a preliminary estimate of the age of the Veritas family (as done in Carruba et al. (2016) for the Karin cluster), and show the necessity to include the Yarkovsky effect in the backward integration in order to improve the convergence. We do this numerically. The maximum Yarkovsky drift in a for a 2 km C-type object, the smallest body in our Veritas sample, is roughly 2.0×10^{-3} au over 8.3 Myr (see Brož et al. (2013) and Sect. 7). For each of the 704 members of the Veritas family we therefore created 11 clones with the same initial

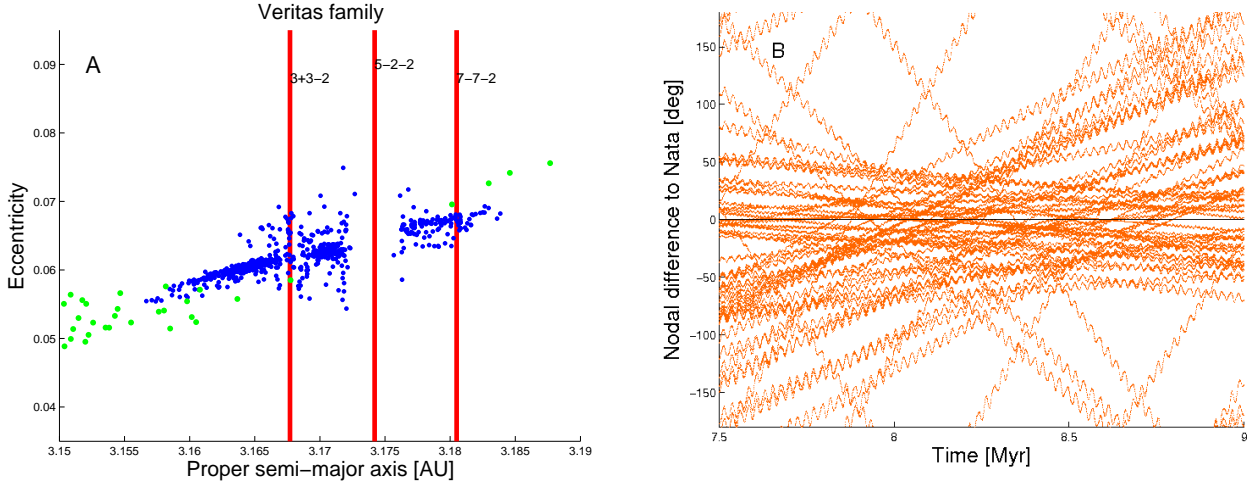


Figure 5. Panel A: an (a, e) projection of Veritas family members (blue full circles) and background asteroids (green full circles) that passed our convergence criterion. Panel B: convergence of the nodal longitudes at $\simeq 8.3$ Myr of the first 50 members of the Veritas family (other members not shown for clarity). The vertical dashed lines display the approximate limits of the Veritas family age.

orbits. Each clone was assigned a drift rate, da/dt , from -3.0×10^{-10} au/yr to 3.0×10^{-10} au/yr, with a step of 0.6×10^{-10} au/yr between individual clones.

The limits of da/dt correspond to the maximum negative and positive total drifts of 2.5×10^{-3} au, i.e. about 25% larger than the maximum expected change in a for the smallest fragment over the estimated age of the family. All 7744 clones were then integrated backward in time over 10 Myr with *SWIFT_RMVS3_DA*, a symplectic integrator based on *SWIFT_RMVS3* code (Levison & Duncan 1994) that was modified by Nesvorný & Bottke (2004) to include a constant drift in the semi-major axis.

The integration was used to refine the age estimate of the Veritas family. Here we only used the past convergence of Ω . For each time output of the integration between 7.9 to 8.6 Myr ago, we computed the standard deviation of $\Delta\Omega$ values (deltas computed with respect to (1086) Nata) for 704 clones of our simulation with *zero* Yarkovsky drift. We then searched for the minimum of the standard deviation of $\Delta\Omega$. Figure 6 displays the time evolution of $\sigma(\Delta\Omega)$ as a function of time for the simulated asteroids. Based on this, the age of the Veritas family was found to be 8.24 ± 0.17 Myr.

Adopting this age, we identified the value of da for each clone that minimizes its $\Delta\Omega$. We found that the convergence in $\Delta\Omega$ is still not perfect, partly because of the rough resolution of da/dt with only 11 clones and partly because many near resonant orbits, which were not filtered out with our Lyapunov time cut, displayed significant chaos. To avoid these problems, we applied a narrower selection of 274 objects, which: (i) have semi-major axes less than 3.166 au (to avoid possible interactions with the 3+3-2 resonance), and (ii) have Lyapunov times greater than 2×10^5 yr, to avoid chaotic orbits. Since one of our goals with this numerical experiment is to verify the possible past convergence of ϖ , we believe that our approach based on selecting the most regular objects in the R_1 region, including (1086) Nata, is justified. For each value of da/dt obtained from the previous simulations, we created 31 additional clones of the same particle with da/dt values covering plus or minus the step

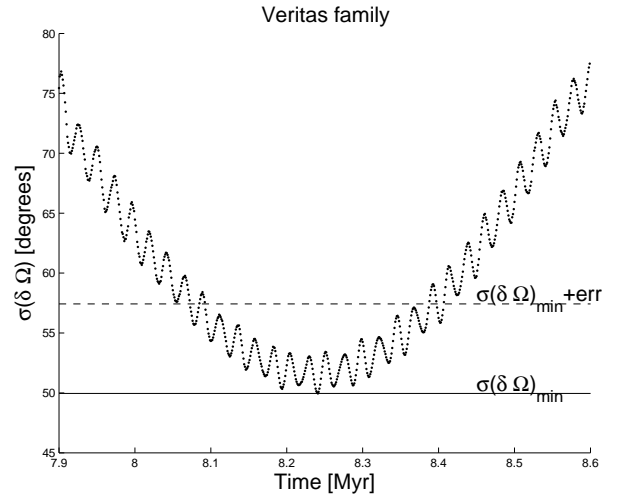


Figure 6. The evolution of the standard deviation of $\Delta\Omega$ as a function of time. The horizontal line identifies the minimum value of $\Delta\Omega$, while the dashed line shows the minimum value plus its error, assumed equal to one standard deviation of the $\Delta\Omega$ values over the length of our integration.

value of 0.6×10^{-10} au/yr used in the previous integration. Overall, we integrated 8494 orbits.

To better identify the orbits whose ϖ angles converge to that of (1086) Nata, we filtered $\Delta\Omega_i = \Omega_i - \Omega_{Nata}$ and $\Delta\varpi_i = \varpi_i - \varpi_{Nata}$, where the suffix i indicates the i -th asteroid, with a low-pass digital Fourier filter (see Carruba (2010) for a description of the filtering method). This removed all frequency terms with periods shorter than 10^5 yr. Fig. 7 illustrates this procedure in an example.

We then analyzed the time behavior of the digitally filtered $\Delta\Omega$ and $\Delta\varpi$ angles. We first obtained a refined age estimate of the Veritas family using two approaches: for each of the 31 clones of a given asteroid, we selected the one with the minimum values of $\Delta\Omega$ and $\Delta\varpi$ at each time step. We then computed χ^2 -like variables using the relationships:

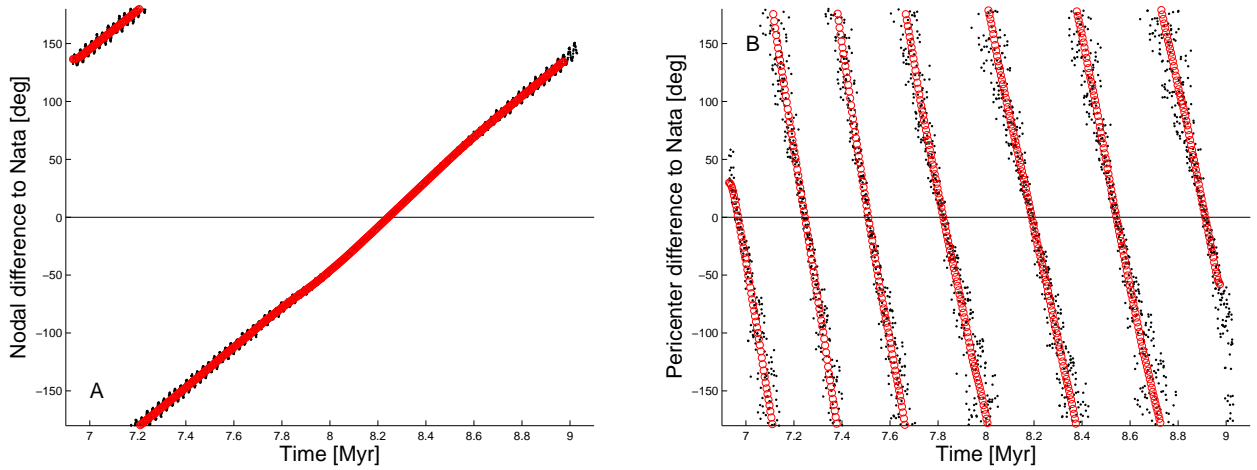


Figure 7. Osculating (black dots) and filtered (red circles) values of $\Delta\Omega = \Omega_{ast} - \Omega_{Nata}$ (panel A), and of $\Delta\varpi = \varpi_{ast} - \varpi_{Nata}$ (panel B), for one of the 8494 integrated particles in the second run. All frequency terms with a period smaller than 10^5 yr were removed in the filtered elements.

$$\chi_1^2 = \sum_{i=1}^{N_{ast}} (\Delta\Omega_i)^2, \quad (4)$$

$$\chi_2^2 = \sum_{i=1}^{N_{ast}} [(\Delta\varpi_i)^2 + (\Delta\Omega_i)^2], \quad (5)$$

where $N_{ast} = 274$ is the number of asteroids in our sample. The first relationship will minimize the dispersion in $\Delta\Omega$, while the second will minimize the dispersion in both $\Delta\Omega$ and $\Delta\varpi$. Since the convergence in $\Delta\Omega$ is more robust, the first method provides a better estimate for the age. We will consistently use results from this first method hereafter. The second method, however, shows that convergence in $\Delta\varpi$ is actually possible, at least in the numerical model here considered.

Fig. 8 displays the time evolution of the square root of these two quantities (see panel A and B). We define the nominal error of $\sqrt{\chi^2}$ as the standard deviation of these quantities over the considered time interval. Based on this analysis, the Veritas family is $8.23^{+0.37}_{-0.31}$ Myr old. It is important to point out that, for the first time, we were also able to obtain the convergence of ϖ . At the nominal family age of $8.33^{+0.22}_{-0.28}$ Myr obtained with the second method, we identified a set of 274 clones whose angles have minimum values of $\Delta\varpi$ and $\Delta\Omega$. The result is shown in Fig. 9: the age solutions of the Veritas family with both methods are statistically identical. Apart from internal consistency, it also justifies the convergence of the longitudes of pericenter. Overall, the convergence of the angles is remarkable: the standard deviations of the distribution in $\Delta\Omega$ and $\Delta\varpi$ at the family nominal age are 8.4° and 8.7° , respectively. Fig. 10 shows histograms of the two distributions. The results obtained with the first method were similar: the standard deviations in this case are equal to 7.7° and 8.9° , respectively.

As a next step, we extracted the semi-major axis drifts da from clones that show the best convergence at the nominal family age. The result is shown in Fig. 11. We also obtained da values at the limits of the age range (7.9 and

8.6 Myr). The distribution of da values is similar in all these cases. As expected from the standard theory on the Yarkovsky effect, the larger asteroids have smaller da values. We discuss this in more detail in Sects. 7 and 8. A list of the 274 studied asteroids with their proper elements $a, e, \sin i$, proper frequencies g and s , Lyapunov exponents LCE , and estimated drift speeds da/dt is given in Table 1, available in its full length in the electronic version of the paper.

6 EFFECTS OF ENCOUNTERS WITH (1) CERES AND (10) HYGIEA

To evaluate the effect that close encounters with massive main belt asteroids may have had on the convergence of the secular angles, we repeated the integration of our selected 274 Veritas members, but this time we also included the gravitational effect of: (i) (1) Ceres, and (ii) both (1) Ceres and (10) Hygiea. The latter asteroid, the fourth most massive in the main belt, was included because of its orbital proximity to the Veritas family and the possible role that the $g - g_{Hygiea}$ secular resonance (see Appendix 1 for a discussion of the possible effect of this resonance).

Fig. 12 shows the distribution of changes of ϖ and Ω in different cases. The da values from the Yarkovsky effect were kept constant in all the three cases. In principle, fine tuning of these values, as performed in the previous section, could compensate the effects of encounters with Ceres and Hygiea, but, since the occurrence of a given encounter with a massive body at a given time depends on the Solar System model used (Carruba et al. 2012), adding more massive bodies to the simulations would require a different fine tuning.

Encounters with Ceres and Ceres/Hygiea increase the standard deviation of the distribution in $\Delta\Omega$ from 8.4° up to 26.2° and 26.0° , respectively. Surprisingly, they completely destroy the convergence in $\Delta\varpi$. Both models cause the standard deviation of the distribution in $\Delta\varpi$ to reach values near 101.3° , corresponding to a uniform distribution. What is causing this remarkable behavior?

Figure 13 show values of $\Delta\varpi$ and $\Delta\Omega$ values as a func-

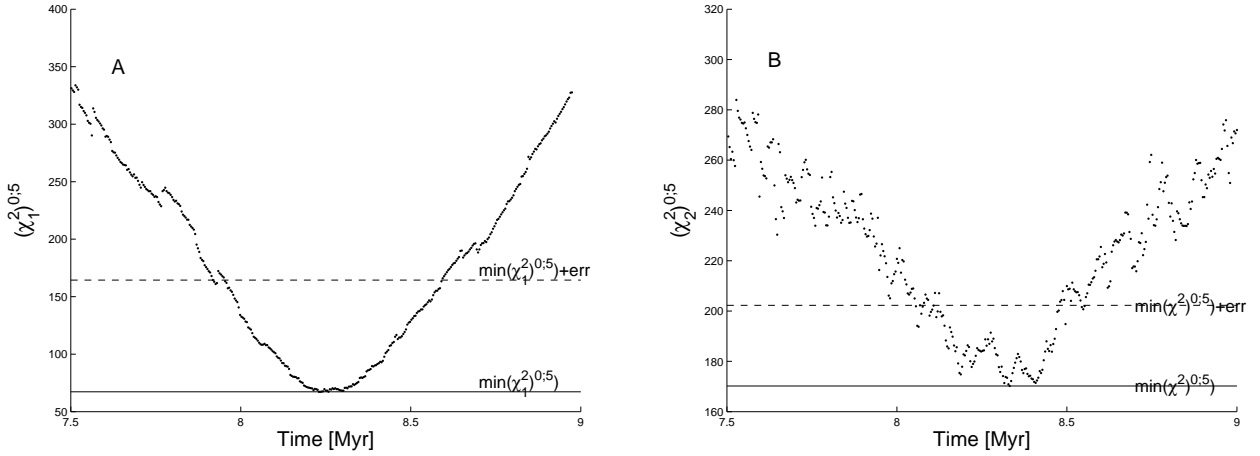


Figure 8. Time evolution of the square root of χ^2 , as defined in Eqs. (4) and (5). The horizontal black line displays the minimum value of these quantities, while the dashed line show the minimum plus the error, defined as square root of the standard deviation of χ^2 over the considered time interval.

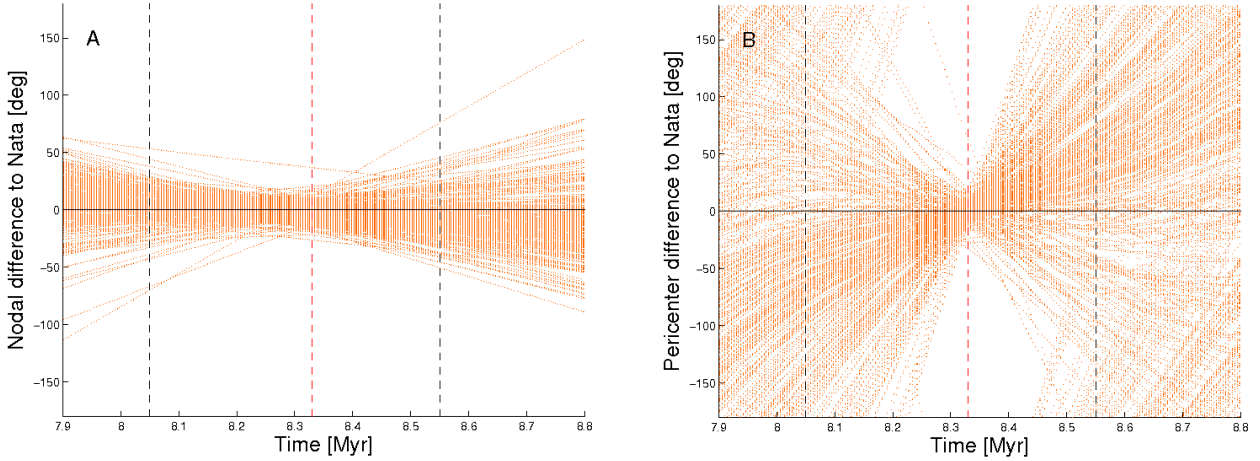


Figure 9. Convergence of filtered $\Delta\Omega$ (panel A) and $\Delta\varpi$ (panel B) for the 274 particles with the lowest values of these angles at the nominal family age. Vertical red line displays the nominal Veritas family age, while the vertical black dashed lines show the possible range of family ages obtained with the χ^2 -like approach of Eq. (5).

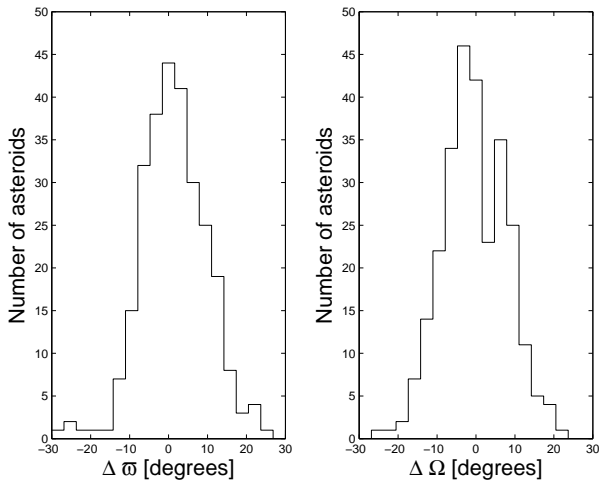


Figure 10. Histograms of the distributions of $\Delta\varpi$ and $\Delta\Omega$ obtained at the family nominal age of 8.33 Myr, computed with our second approach.

tion of time for (1086) Nata with respect to a reference case where no massive asteroids were included in the integration. It can be noted that while changes in $\Delta\Omega$ are smaller than 30° in both models, changes in $\Delta\varpi$ are bigger than 180° in the first model, and two complete circulations of this angle were observed in the second model. We can also observe that the time behavior of the angles is different in the two models. While $\Delta\varpi$ increases in the first model, it decreases in the second one (and vice versa for $\Delta\Omega$).

Let us now try to understand what makes the secular angle convergence in the Veritas family so sensitive to gravitational perturbations of massive asteroids, and what it implies for the realistic uncertainty in our determination of the drift rates caused by the Yarkovsky effect. Our method is as follows.

The massive asteroids may affect the nominal convergence of secular angles in two ways: (i) a direct contribution to the secular frequencies s (node) and g (pericenter), or (ii) an indirect effect, which consists of perturbations of the semi-major axis a , being then reflected in nodes and pericenters via dependence of s and g on a . We believe the latter

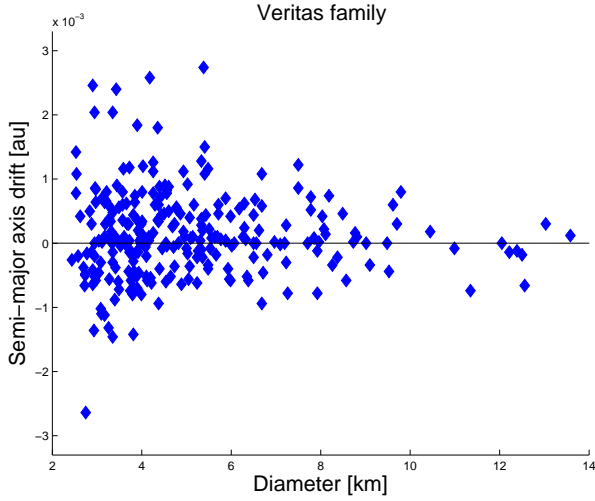


Figure 11. Semi-major axis drift da of Veritas family members over the estimated age of the Veritas family (8.23 Myr). The drifts tend to be smaller for larger members, as expected from the size-dependency of the Yarkovsky effect.

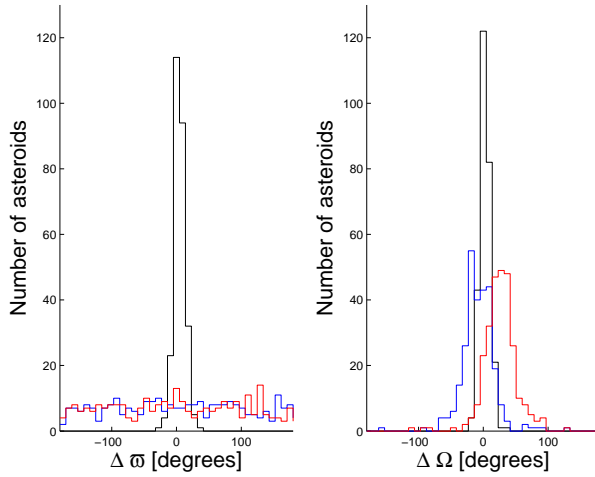


Figure 12. Distribution of changes in ϖ and Ω for the 274 integrated asteroids for the case without Ceres and Hygiea (black line), with Ceres (blue line), and with Ceres and Hygiea (red line).

is dominant, and we will try to demonstrate it in the case of Ceres' influence. Obviously, the effect is larger in the longitude of pericenter just because the gradient $\partial g/\partial a$ is nearly an order of magnitude larger than $\partial s/\partial a$ in the Veritas family (see, e.g., Appendix 1).

We postulate that the nature of Ceres' perturbation in semi-major axis of Veritas orbits is due to stochastic jumps during sufficiently close encounters. These are favored by two facts: (i) the orbit pericenter q for Veritas orbits is close to the orbit apocenter Q of Ceres, and (ii) the mean inclination of Veritas orbits is nearly the same as the mean inclination of Ceres' orbit. To probe how (i) and (ii) influence circumstances of close encounters to Ceres, we used the Öpik theory to compute intrinsic collision probability p_i of the two orbits. Indeed, we obtained $p_i \simeq 3.5 \times 10^{-17} \text{ km}^{-2} \text{ yr}^{-1}$, which is slightly times larger than the average in the main belt (e.g., Bottke et al. (1994)).

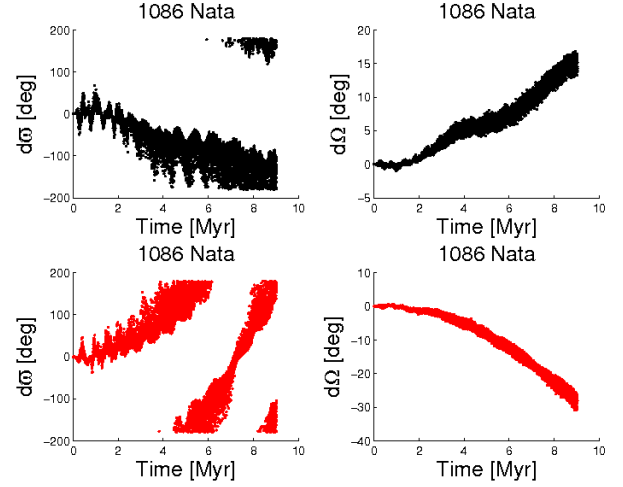


Figure 13. $\Delta\varpi$ and $\Delta\Omega$ values as a function of time for (1086) Nata when Ceres was considered as a massive perturber (top panels, black dots) and when Ceres and Hygiea were both considered as perturbers (bottom panels, red dots). The values were computed relative to a reference case where no massive asteroid perturbers were included in the integration.

Given the difference of s frequencies of Veritas members and Ceres, we note that every $\simeq 60$ kyr the orbital planes get very close to each other. These are the moments when the instantaneous collision probability with Ceres becomes even larger than the average stated above. Obviously, in order for a close encounter to really happen, Ceres must be close to its aphelion and Veritas member close to its perihelion. The difference in g frequencies is much larger than in s frequencies, so the timescale of very favorable collision probability of Veritas members to Ceres is $\simeq 60 \times (360/5)$ kyr or $\simeq 4$ Myr (assuming, for simplicity, that in the Ceres orbital plane the orbit of Veritas members must be oriented within $\simeq 5^\circ$ with respect to the optimum aphelion-perihelion configuration). Therefore, during the estimated age of Veritas family, a typical member may undergo up to three such close encounters to Ceres. This is consistent with data in the top and right panel of Fig. 13. Note that the additional nodal drift of (1086) Nata underwent two changes of rate at approximately 3 Myr and again at about 6.5 Myr.

Obviously, none of the currently observed Veritas members impacted Ceres during its lifetime. We may, however, estimate an order of magnitude of its closest approach R_{app} . Considering again the Öpik-theory approach, the condition for R_{app} reads: $p_i R_{\text{app}}^2 T \simeq 1$, where $T = 8.3$ Myr the age of the family. Using this relation we obtain $R_{\text{app}} \simeq 5.6 \times 10^5$ km. This result is averaged over all possible orbit configurations. Assuming special coplanarity and alignment conditions would have a much larger collision probability, we may assume the really closest approaches of Veritas fragments to Ceres that occurred few times in the past had $R_{\text{app}} \simeq 10^4$ km.

Finally, we estimate the magnitude of orbital semi-major axis jump δa of Veritas member during such a close encounter with Ceres. Obviously, the result depends on details of the encounter. However, here we are interested in obtaining the order of magnitude result only. Assuming the change in binding energy to the Sun is of the or-

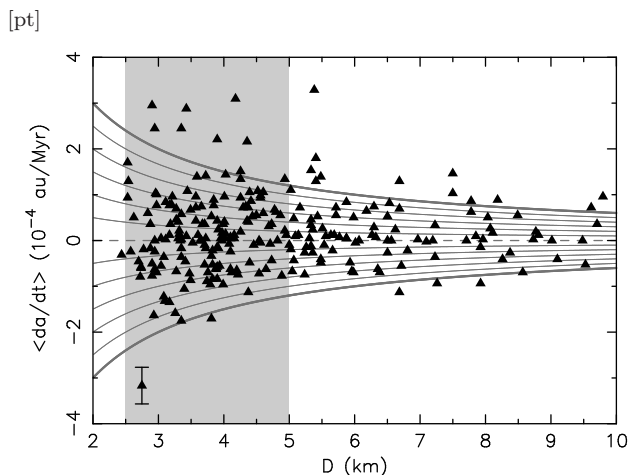


Figure 14. Adjusted semi-major axis drift rates da/dt to achieve optimum convergence in secular angles of 264 $D < 10$ km asteroids in the R_1 region of Veritas family versus their estimated size D . The values correspond to the formal best fit solution minimizing χ^2 in Sect. (5) at 8.23 Myr. The thick gray lines correspond to our estimate of maximum values of the Yarkovsky effect for nominal physical parameters, or $\pm 2.4 \times 10^{-4}$ au Myr $^{-1}$ at $D = 2.5$ km (see Fig. 15) and the characteristic $\propto 1/D$ size dependence. The thin gray lines for respectively smaller da/dt values at the reference size of 2.5 km. The uncertainty interval in da/dt shown for the outlying data-point at the bottom left corner applies to all data. This is our estimated realistic value that takes into account: (i) formal variation of da/dt within the sigma interval of the Veritas family age solution (Fig. 8, panel A), and (ii) the stochastic effect of Ceres and Hygiea close encounters on behavior of the longitude of node and pericenter of asteroids in the Veritas family. The light-gray rectangle indicates the size range 2.5 to 5 km used for our analysis in Sec. 5.

der of magnitude of potential energy in the Ceres gravitational field at the moment of the closest approach, we have $(\Delta a/a) \simeq (M_1/M_0)(a/R_{\text{app}})$, where M_0 and M_1 are the masses of the Sun and Ceres and a is semi-major axis of the Veritas fragment. We obtain $\delta a \simeq 7 \times 10^{-5}$ au in one encounter. If statistically two such encounters may happen the accumulated Δa becomes about 10^{-4} au.

To tie this information to our previous results we note that the characteristic accumulated change in semi-major axis of small Veritas members to achieve orbital convergence is $\simeq (5 - 10) \times 10^{-4}$ au (see Fig. 11). While a part of this value may be due to stochastic effects of Ceres encounters, the main effect is likely due to other dynamical phenomenon. We favor the Yarkovsky effect and discuss details in Secs. 7 and 8. In this respect, however, the random component due to encounters to Ceres and other massive objects in the belt represents a noise. Given the estimates above, its realistic level is $\simeq 1.3 \times 10^{-5}$ au Myr $^{-1}$ in the mean drift rate due to Ceres along. To stay realistic, we shall assume three times larger value to account for the effects of other massive bodies such as (10) Hygiea.

7 EXPECTED DRIFT-RATE IN SEMI-MAJOR AXIS DUE TO THE YARKOVSKY EFFECT

For convenience of discussion in this Section, we express the empirical accumulated change in semi-major axis in $\simeq 8.23$ Myr of the Veritas family age shown in Fig. 11 in terms of the equivalent mean rate. This is shown in Fig. 14. Here we pay attention to the consistency of these values with the predictions from the Yarkovsky effect theory. In particular, we estimate the expected values of to the Yarkovsky effect for these bodies and compare them with the empirical values required by orbital convergence discussed in Sec. 5. A general information about the theory of the Yarkovsky effect may be found in Bottke et al. (2006) or Vokrouhlický et al. (2015). Here we only summarize few facts needed for our application.

While in principle there is only one Yarkovsky effect acting on the body as such, it is customary to divide it into diurnal and seasonal components. Recall that the thermal response of the body surface on solar heating is frequency-dependent and there are typically two primary frequencies involved (unless tumbling rotation state that we disregard in this study): (i) rotation frequency ω , and (ii) revolution frequency (or mean motion) n about the Sun. In virtually all asteroid applications $\omega \gg n$. In this limit, we may consider the thermal effects related to ω (the diurnal component) and those related to n (the seasonal component) frequencies separately. Their mutual interaction is negligible (see, e.g., Vokrouhlický (1999)). In applications of the Yarkovsky effect to the motion of small asteroids only the diurnal component has been considered so far, while the seasonal component has been neglected. There are two reasons that justified this approach. First, in the limit of very low-enough surface thermal inertia values, appropriate for multi-kilometer and larger asteroids in the main belt whose surfaces are expected to be covered with fine regolith layer, the magnitude of the seasonal effect becomes $\simeq \sqrt{n/\omega}$ smaller than that of the diurnal effect. Second, the seasonal effect may become important only for a restricted interval of obliquity values near 90° . For evolved-enough populations of asteroids, the Yarkovsky-O'Keefe-Radzievskii-Paddack (YORP) effect makes the obliquity pushed towards the extreme values 0° or 180° (e.g., Bottke et al. (2006) or Vokrouhlický et al. (2015)) where the seasonal Yarkovsky effect becomes nil. However, in the case of Veritas fragments, none of these arguments might be satisfied. Thermal inertia of fresh, C-type objects might be anomalously large, compared to the data of all asteroids. In the same time, the YORP effect likely did not have enough time to push the obliquity values of the currently observed Veritas members to their asymptotic values (see also Sec. 7.1). As a result, we include both the diurnal and the seasonal components of the Yarkovsky effect in our analysis.

Given only the moderate value of the orbital eccentricity of the Veritas family members, we restrict to the Yarkovsky model applicable to circular orbits. This is sufficient, because the eccentricity corrections to the mean orbital change in semi-major axis are only of the second order in e . At the same time, we limit ourselves to the analytic model for the spherical shape of the asteroids and linearized boundary conditions of the heat conduction. While approximate, the main advantage is that we thus dispose of simple an-

alytic formulas for the secular long-term change of the orbital semi-major axis. Finally, we note that the penetration depth ℓ of the thermal wave for both diurnal and seasonal effects is much smaller than the characteristic radius R of the known Veritas members (ℓ being at maximum few meters even for the seasonal effect; e.g., [Bottke et al. \(2006\)](#); [Vokrouhlický et al. \(2015\)](#)). In this case, we neglect corrections of the order $\propto \ell/R$ or higher in our analysis.

Using all these approximations, we find that the mean semi-major axis drift-rate due to the diurnal variant of the Yarkovsky effect is given by

$$\left(\frac{da}{dt}\right)_{\text{diu}} \simeq \frac{4\alpha \Phi}{9} \frac{\Theta}{n} \frac{\Theta}{1 + \Theta + \frac{1}{2}\Theta^2} \cos \gamma, \quad (6)$$

where $\alpha = 1 - A$, with A the Bond albedo, $\Phi = (\pi D^2 F)/(4mc)$, with the size (diameter) D of the body, $F \simeq 136.3 \text{ W/m}^2$ the solar radiation flux at the mean heliocentric distance of the Veritas family, m the mass of the body, c is the velocity of light, and n the orbital mean motion. Note that $\Phi \propto 1/D$, which implies the Yarkovsky effect magnitude is inversely proportional to the asteroid size. Therefore it is negligible for large Veritas members such as (1086) *Nata*, but becomes important as soon as D becomes smaller than $\simeq 5 - 10 \text{ km}$. Similarly, denoting ρ the bulk density of the asteroid, one has $\Phi \propto 1/\rho$, again the inverse proportional scaling with this parameter. The thermal parameter $\Theta = \Gamma\sqrt{\omega}/(\epsilon\sigma T_*^3)$ depends on of the surface thermal inertia Γ , the rotation frequency ω , the surface infrared emissivity ϵ , the Stefan-Boltzmann constant σ and subsolar temperature $T_* = [\alpha F/(\epsilon\sigma)]^{1/4}$. Finally, γ is the obliquity of the asteroid spin axis.

Using the same notation as above, the mean semi-major axis drift-rate due to the seasonal component of the Yarkovsky effect reads

$$\left(\frac{da}{dt}\right)_{\text{sea}} \simeq -\frac{2\alpha \Phi}{9} \frac{\bar{\Theta}}{n} \frac{\bar{\Theta}}{1 + \bar{\Theta} + \frac{1}{2}\bar{\Theta}^2} \sin^2 \gamma. \quad (7)$$

This is very similar to (6), except for the diurnal thermal parameter Θ now replaced with its seasonal counterpart $\bar{\Theta} = \Gamma\sqrt{n}/(\epsilon\sigma T_*^3)$. Note that the only difference consists in the rotation frequency ω being substituted with the orbital mean motion n . Thus $\bar{\Theta}$ is always smaller than Θ since $\bar{\Theta}/\Theta = \sqrt{n}/\omega$. Importantly-enough, the diurnal and seasonal effects have also different dependence on the rotation pole obliquity γ , the former being maximum at $\gamma = 0^\circ$ and 180° , the latter at $\gamma = 90^\circ$. Hence, the aforementioned YORP-driven depletion of the obliquity distribution at mid- γ values contributes to dominance of the diurnal effect. However, when the YORP effect does not have enough time to modify obliquity values, as we check in the next section, there is no obvious reason to neglect the role of $\gamma \simeq 90^\circ$ obliquity values.

The total rate in semi-major axis is simply $da/dt = (da/dt)_{\text{diu}} + (da/dt)_{\text{sea}}$. For a given body, da/dt depends on a number of physical parameters described above. In some cases the dependence conforms to a simple scaling. Thus, $da/dt \propto \Phi \propto 1/(D\rho)$. For other parameters the dependence is less obvious and needs to be explored numerically. This is the case of the surface thermal inertia Γ , rotation frequency ω and obliquity γ . Obviously, we do not know any of these values for small members in the Veritas family. It is not, however, our intent here to speculate about individual

bodies in the Veritas family. Rather, by comparison with the derived da/dt values in Sec. 5, we may be only able to say something about distribution of these parameters in the whole sample of small Veritas members.

To assist with this goal, we performed the following numerical experiment which may serve as a template for comparison with real Veritas data. Figure 15 shows results where we fixed a reference asteroid size $D = 2.5 \text{ km}$, bulk density $\rho = 1.3 \text{ g cm}^{-3}$ and rotation period 6 hr (implying thus $\omega \simeq 2.9 \times 10^{-4} \text{ rad s}^{-1}$). The chosen size corresponds to that of the smallest Veritas members, for which we were able to determine da/dt value from the secular angles convergence (Fig. 14). The assumed bulk density is the best guess for the C-type taxonomy of the Veritas family (e.g., [Scheeres et al. \(2015\)](#)). Two more parameters remain to be selected for predicting the Yarkovsky value of da/dt , namely the surface thermal inertia Γ and obliquity γ . For the latter, we assume an isotropic distribution of the spin axes in space. This is, in fact, the underlying hypothesis that we are going to test in comparison with the data. For the former, we assumed a log-normal distribution with two different mean values of 100 SI units (left panel) and 250 SI units (right panel). Both values are within the expected range of thermal inertia values of small, C-type asteroids (Fig. 9 of [Delbò et al. \(2015\)](#)).

The maximum range of possible da/dt values due to the Yarkovsky effect spans, for the chosen parameters, from about $-2.4 \times 10^{-4} \text{ au Myr}^{-1}$ to $2.4 \times 10^{-4} \text{ au Myr}^{-1}$. Given the 6 hr rotation period it corresponds to 0° or 180° obliquity values and $\Gamma \simeq 50$ in SI units. These limits would be the same for other rotation periods, because the diurnal Yarkovsky effect, the only component contributing at extreme obliquity values, is invariant when Γ and ω change preserving $\Gamma\sqrt{\omega}$ value (see Eq. 6). So for longer rotation periods the optimum thermal inertia would just slightly shift to the larger values. These maximum values favorably compare with majority of our solved da/dt values for small fragments in the Veritas family (Fig. 14). The few outliers beyond these limits, may be bodies residing on slightly unstable orbits for which our analysis is not so accurate (for instance due to close encounters to Ceres or Hygiea, or secular effects due to these massive bodies in the main belt). Alternately, these cases may also correspond to anomalously low-density fragments, or bodies for which the absolute magnitude has not been determined accurately and they actually have quite smaller size.

The Yarkovsky effect at 90° obliquity is the pure seasonal contribution. At low Γ values this component is basically nil, but at $\Gamma \simeq 700$ in SI units it rivals the maximum value of the diurnal effect. At still reasonable Γ values between 300 and 400 in SI units its contribution is not negligible and needs to be taken into account. The contribution of the seasonal effect makes the total Yarkovsky da/dt value at generic obliquities, such as 60° or 120° on Fig. 15, bent toward negative values for sufficiently large thermal inertia, breaking thus the symmetry between the positive and negative da/dt values.

Let us assume a population of Veritas fragments with an isotropic distribution of spin axes and log-normal tight distributions of Γ values shown by the top histograms on the left and right panels of Fig. 15. The histograms along the right ordinate then indicate what would be the distribution

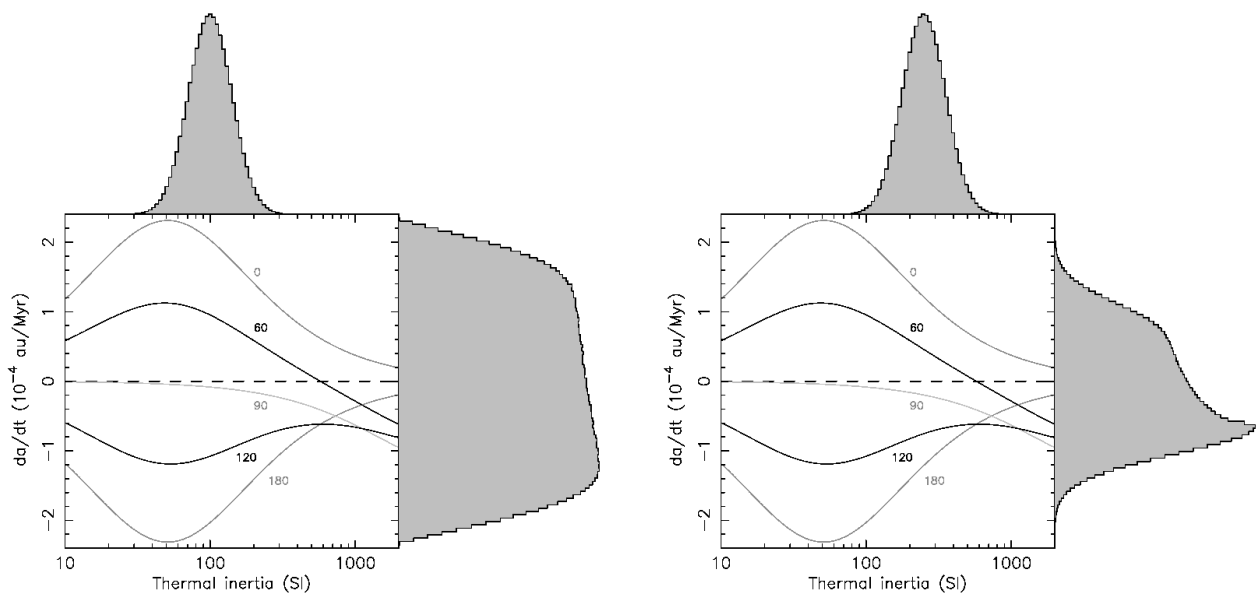


Figure 15. The middle part on the left and right panels shows dependence of the total semi-major axis drift-rate due to the Yarkovsky effect on the surface thermal inertia Γ (we assumed $D = 2.5$ km size member in the Veritas family with a rotation period of 6 hr and a bulk density $\rho = 1.3$ g cm $^{-3}$). Different curves for five representative values of the obliquity $\gamma = 0^\circ, 60^\circ, 90^\circ, 120^\circ$ and 180° (labels). Assuming a population of bodies with a log-normal distribution of Γ values shown by the top histograms, and isotropic distribution of spin axis orientations in space, one would obtain distributions of the da/dt values shown on the right side of each of the panels. The difference between left and right is in the mean value of Γ : 100 SI units on the left and 250 SI units on the right.

of da/dt values for this sample. As already expected, the contribution of the seasonal Yarkovsky effect makes it that in both cases the negative da/dt values are more likely. However, for low thermal inertia values (left panel), the asymmetry is only small, 52.4% vs 47.6% of all cases only. This asymmetry becomes more pronounced for larger thermal inertia values (right panel), for which 59.2% cases have da/dt negative and only 40.8% cases have da/dt positive. Playing with more assumptions about the thermal inertia distributions one may thus create other templates for the da/dt distributions for samples of fragments that have their spin axes isotropically distributed in space.

Obviously, if none of such templates corresponds to the observed distribution of da/dt values in the Veritas family, the underlying assumption of isotropy of the rotation axes must be violated. With only limited data, and a lack of information about fragments other physical parameters, we cannot solve for the spin axis distribution, but at least say some trends. This is the goal of our analysis in Sec. 7.1.

7.1 A possible role of the YORP effect?

Before we proceed with comparison of the observed and modeled da/dt values, we pay a brief attention to the neglected role of the YORP effect. In particular, we assumed that the ≈ 8.3 Myr age of the Veritas family is short enough that the YORP torques did not result in a significant change of obliquity γ of its members (such that γ could be considered constant in our analysis). This may look odd at the first sight, because the Yarkovsky and YORP effects are just two faces of one physical phenomenon, namely the recoil effect of thermally re-radiated sunlight by the asteroid surface.

The key element in understanding this issue is a different dependence on the size D . While the Yarkovsky effect is

only inversely proportional to D ($da/dt \propto 1/D$, see above), the YORP effect is inversely proportional to D^2 . As a result, its importance decreases much faster with increasing size of the bodies.

The model predictions of the YORP effect are much less certain than those of the Yarkovsky effect (see, e.g., discussion in Vokrouhlický et al. (2015)). In this situation we rather use real data from the Karin family (Carruba et al. 2016), and re-scale them to the case of the Veritas family. This simple re-scaling procedure must take into account different heliocentric distances ($a \approx 2.86$ au vs $a \approx 3.16$ au), bulk densities ($\rho \approx 2.5$ g cm $^{-3}$ vs $\rho \approx 1.3$ g cm $^{-3}$) and ages ($T \approx 5.8$ Myr vs $T \approx 8.3$ Myr). The accumulated change $\Delta\gamma$ in obliquity scales with $\propto T/(\rho a^2 D^2)$. This makes us to conclude that $D \approx 2$ km Karin asteroids should accumulate about the same obliquity change as $D \approx 3$ km Veritas asteroids (the smaller bulk density and larger age playing the main role). Looking at Fig. 5 of Carruba et al. (2016), we conclude that the YORP effect is negligible for those sizes (as it has been also verified in that paper). Since $D \approx 3$ km are about the smallest asteroids we presently observe in the Veritas family, the omission of the YORP effect in this study is justified. For sake of comparison we note, that the population of $D \approx 1.4$ km Karin asteroids already revealed traces of the YORP effect (Fig. 5 in Carruba et al. (2016)). Therefore we predict that, when the future observations will allow to discover $D \approx 2$ km members in the Veritas family, we should start seeing similar YORP pattern as in the Karin family (i.e., depletion of the $da/dt \approx 0$ values).

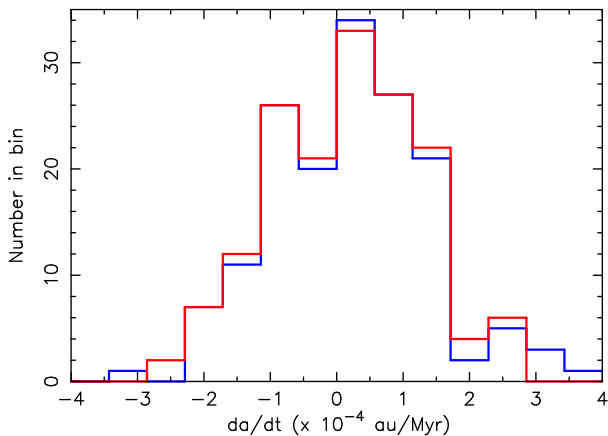


Figure 16. Result of a formal fit of the observed da/dt values for 160 Veritas members with estimated size ≤ 5 km all mapped to a reference size of 2.5 km using the $\propto 1/D$ scaling (blue histogram). The bin width, $\simeq 0.6 \times 10^{-4}$ au Myr $^{-1}$, is only slightly smaller than the estimated realistic uncertainty of the da/dt values of individual asteroids because of the effect of massive bodies in the main belt. The red histogram is a best-fit from a simulation, where we assumed (i) isotropic distribution of rotation poles, (ii) rotation period 7 hr, (iii) mean surface thermal inertia 158 in SI units, and (iv) bulk density 1.07 g cm $^{-3}$.

8 COMPARISON OF THE OBSERVED AND MODELED YARKOVSKY DRIFT VALUES

Here we describe the sample of the solved-for values of the Yarkovsky drift da/dt from Sec. 5 in some detail. However, the reader is to be warned upfront that we show here just an example of many possible solutions. The data are simply not constraining the model enough at this moment.

We already observed the overall consistency of the maximum determined da/dt with the Yarkovsky prediction for the sizes of Veritas members. Here we consider a sub-sample of 190 asteroids with size $D \leq 5$ km. This is because data for small enough asteroids should enable a better description of the Yarkovsky effect and be less contaminated in a relative sense by the perturbation from Ceres and massive asteroids. We use the inverse-proportional relation between da/dt and D and map all these values to the reference size $D_{\text{ref}} = 2.5$ km. This corresponds to the smallest-observed Veritas members (Fig. 14). The blue histogram at Fig. 16 shows distribution of these mapped values. We used $\simeq 0.6 \times 10^{-4}$ au Myr $^{-1}$ width of the bins for two reasons: (i) the number of asteroids in the sample is not very large, and (ii) the realistic uncertainty of the individual da/dt solutions is $\simeq \pm 0.4 \times 10^{-4}$ au Myr $^{-1}$, only slightly larger than the bin. The latter is mainly due to the stochastic effect of close encounters with Ceres and Hygiea (Sec. 6). Therefore it does not make sense to use smaller bin-size. There are 95 objects with $da/dt > 0$, and only 65 with $da/dt < 0$, in our sample. At the first sight, this precludes a possibility of isotropic distribution of spin axes (see discussion in Sec. 7). However, we demonstrate below that the small statistics of bodies still allows to match the data with the underlying pole isotropy. Obviously, solutions with anisotropic pole distribution are also possible, but these are not attempted here, because they would involve many more unconstrained degrees of freedom in the model.

We conducted the following simple numerical experiment. Considering 160 $D = D_{\text{ref}} = 2.5$ km size members of the Veritas family, we randomly sampled a three-dimensional parametric space of (i) characteristic rotation period P values (given the same to all bodies), (ii) mean surface thermal conductivity $\bar{\Gamma}$ with a tight log-normal distribution with standard deviation of 0.1 in $\log \Gamma$ (see the top histograms on Fig. 15, and (iii) bulk density ρ . The tested interval of values were: (i) 4 hr to 20 hr for P , (ii) 50 to 1000 in SI units for $\bar{\Gamma}$, and (iii) 0.8 to 1.5 g cm $^{-3}$ for ρ . We performed 25000 trials of a random sampling of this parametric space. For each these choices, we then let the code test 10^4 random variants of spin axes obliquities. Altogether, we thus ran 2.5×10^8 simulations. In each of them we computed the distribution of da/dt values for the sample using Eqs. (6) and (7). We evaluated the formal $\chi^2 = \sum (N_c - N_o)^2$ measure of the difference between the data N_o and the model N_c using the bins shown in Fig. 16. In particular, we considered only the ten central bins around zero up to da/dt values of $\pm 2.5 \times 10^{-4}$ au Myr $^{-1}$, because these are maximum expected Yarkovsky values (e.g., Fig. 15). The solution is largely degenerate, since many parameter combinations resulted in reasonable fits, so we restrict here to summarize just the main trends. These are best shown by a projection of the χ^2 values onto the plane of surface thermal inertia $\bar{\Gamma}$ and bulk density ρ (Fig. 17).

We note that the reasonable matches required: (i) $\bar{\Gamma}$ smaller than $\simeq 400$ SI units, and most often being in the interval between 150 and 250, (ii) rotation period values P are not constrained (thus no shown in the Fig. 17), and (iii) the density ρ should be smaller than 1.3 g cm $^{-3}$. The reason for (i) is explained in Sec. 7: larger thermal conductivity would necessarily prefer negative values of da/dt which is not observed in our data. Actually the predominance of the positive da/dt is achieved only as a result of statistical noise on low-number of data in the individual bins. The low densities are required to match the observed minimum to maximum range of da/dt values.

9 CONCLUSIONS

Our results can be summarized as follows:

- We identified and studied the members of the Veritas family and asteroids in the family background. As in Tsiganis et al. (2007), we found that the chaotic orbits with Lyapunov times $< 10^5$ yr are in the 3+3-2 and 5-2-2 three body resonances. (490) Veritas itself is currently in the 5-2-2 resonance and is characterized by a very short Lyapunov time. With a possible exception of the $g - g_{\text{Hygiea}}$ secular resonance, secular dynamics plays only a minor role in the region of the Veritas family
- We studied physical properties of asteroids in the Veritas family region. The Veritas family is mostly made of C-type objects of low albedo. The mean albedo value of the Veritas family is 0.07. Among Veritas members, only (490) Veritas and (1086) Nata have masses larger than 10^{17} kg. The mass distribution of the family is consistent with the outcome of a fragmentation event.
- We investigated the past convergence of nodal longitudes of members of the Veritas family with Lyapunov times $> 3 \times 10^4$ yr and refined the list of secure Veritas family

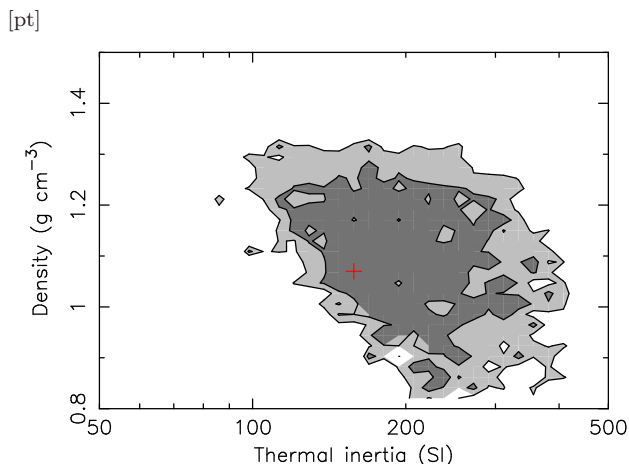


Figure 17. Region of admissible χ^2 values in the parametric space surface thermal inertia $\bar{\Gamma}$ (abscissa) and bulk density ρ (ordinate) of the Veritas-family members. The χ^2 is a measure of a success to match distribution of the Yarkovsky rate of change of the semimajor axis da/dt obtained for 160 $D \leq 5$ km asteroids in the R₁ region of the family (see the text). At each grid-point in the plane we also tested rotation periods between 4 hr and 20 hr and we run 10^4 trials of isotropically distributed spin axes of the fragments. The light gray area shows where $\chi^2 \leq 40$, the dark gray area shows where $\chi^2 \leq 30$. The formally best-fit value $\chi^2 = 13$, shown by red cross, corresponds to $\bar{\Gamma} = 158$ (SI units), $\rho = 1.07$ g cm⁻³, and $P = 7$ hr (see Fig. 16).

members. 704 asteroids have their nodal longitude converging to within $\pm 60^\circ$ to that of (1086) Nata between 8.1 and 8.5 Myr ago.

- By performing two sets of numerical integrations with the Yarkovsky force, we found that the inclusion of the Yarkovsky effect is crucial for improving the convergence. The convergence of nodal longitudes of 274 most regular members of the Veritas family is almost ideal. The best age estimate is $8.23^{+0.37}_{-0.31}$ Myr.

- For the first time, we were able to demonstrate the possibility of convergence of the perihelion longitudes. Regrettably, the effect of close encounters with Ceres and other massive main belt asteroids destroys the convergence in ϖ , and also defocuses the convergence of Ω . This limits the accuracy of our Yarkovsky drift estimates to $\pm 4 \times 10^{-5}$ au/Myr.

- To within this precision, we were able to obtain da/dt drift rates for 274 members of the Veritas family. The drift rates are larger for smaller asteroids, as expected from the Yarkovsky effect. The inferred distribution of da/dt values is consistent with a population of objects with low-densities and low thermal conductivities.

- The effects of YORP cannot be discerned in the Veritas family. They should become apparent when future observations will help to characterize the family members with $D < 2$ km.

In summary, despite the very complex dynamical environment of the Veritas family, we were able to refine the family age estimate, obtain Yarkovsky drift rates for 274 family members, and constrain several key parameters such as their bulk density and thermal conductivity. Results are consistent with the standard theory of the Yarkovsky effect.

ACKNOWLEDGMENTS

We are grateful to the reviewer of this paper, Prof. Andrea Milani, for comments and suggestions that significantly improved the quality of this work. We would like to thank the São Paulo State Science Foundation (FAPESP) that supported this work via the grant 16/04476-8, and the Brazilian National Research Council (CNPq, grant 305453/2011-4). VC was a visiting scientist at the Southwest Research Institute (SWRI) during the preparation of this paper. DV's work was funded by the Czech Science Foundation through the grant GA13-01308S. DN's work was supported by the NASA SSW program. This publication makes use of data products from the Wide-field Infrared Survey Explorer (WISE) and Near-Earth Objects (NEOWISE), which are a joint project of the University of California, Los Angeles, and the Jet Propulsion Laboratory/California Institute of Technology, funded by the National Aeronautics and Space Administration.

10 APPENDIX 1: PROPER FREQUENCIES BEHAVIOR IN THE VERITAS REGION

Following the approach of Nesvorný & Bottke (2004) we attempt to compute the drift rates caused by the Yarkovsky effect based on the values of $\Delta\Omega$, the difference between the values of Ω between those of the 705 members of the Veritas family and those of (1086) Nata itself. For this purpose, we first need to determine how the g and s proper frequencies depend on proper semi-major axis in the Veritas region. Contrary to the case of the Karin cluster, we cannot use for the Veritas family the convergence of the past longitudes of the nodes ϖ , since the Veritas family is too close to the 2/1 mean-motion resonance with Jupiter, and this causes the precession of the longitude of the nodes to increase significantly. According to Nesvorný & Bottke (2004), values of $\Delta\Omega_{P,j}$ for a given j member at each given time $t = -(\tau + \Delta t)$, with τ the estimated age of the Karin group, is given by:

$$\Delta\Omega_{P,j}(t) = \Omega_{P,j}^* - \Omega_{P,1}^* - \frac{1}{2} \frac{\partial s}{\partial a_P} (\delta a_{P,j} - \Delta a_{P,1}) \tau - (s_j - s_1) \Delta t, \quad (8)$$

where $\Omega_{P,j}^* - \Omega_{P,1}^*$ is the proper nodal longitude difference caused by the ejection speeds ΔV , and assumed negligible hereafter (Nesvorný & Bottke (2004) estimate that it is of the order of 1° for the Karin cluster, and should not be much larger for the Veritas family). $\frac{\partial s}{\partial a_P}$ define how frequencies change with a_P . Nesvorný & Bottke (2004) used the analytic perturbation theory of Milani & Knežević (1994) to estimate this rate equal to -70.0 arcsec/yr/au for all Karin cluster members (with an uncertainty of 1% caused by the spread in proper a_P of the cluster members). The case of the Veritas family is, however, much more challenging.

Fig. 18 displays an (a, s) projection of members of the Karin cluster (panel A) and of the Veritas family (panel B). While indeed most Karin members follows a single line of constant $\delta s / \delta a$ in the (a, s) plane, the distribution of (a, s) for the Veritas family is much more disperse. The local three-body resonances play an important role in affecting the values of asteroid proper in the region of the Veritas family, in a way not observed for the Karin cluster. To investigate

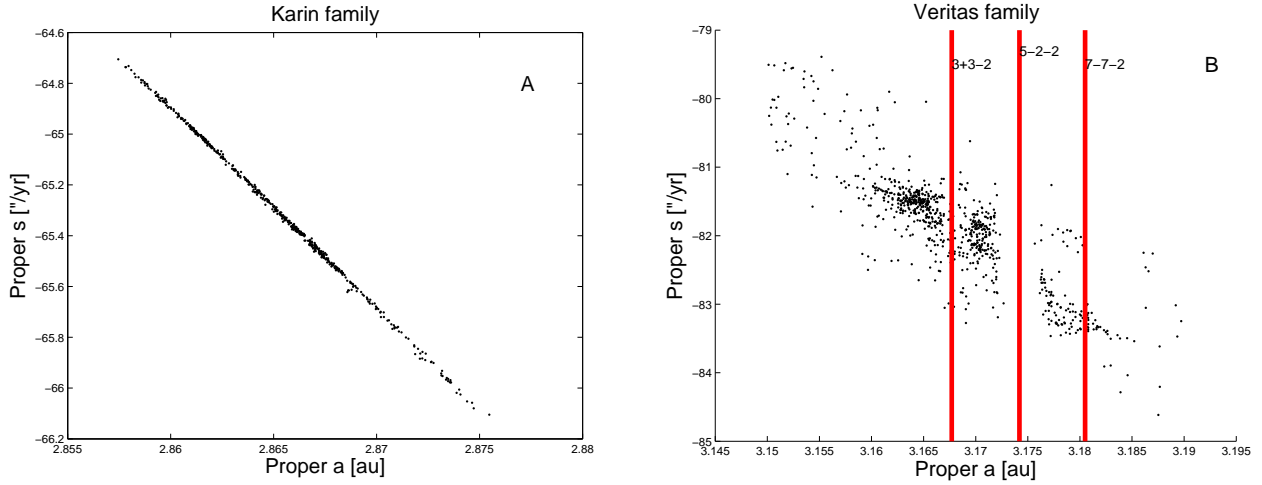


Figure 18. An (a, s) projection of members of the Karin cluster (panel A) and of the Veritas family (panel B). While the (a, s) distribution of the Karin cluster members mostly follows a single line of constant $\delta s/\delta a$, the same distribution for the Veritas family is much more dispersed.

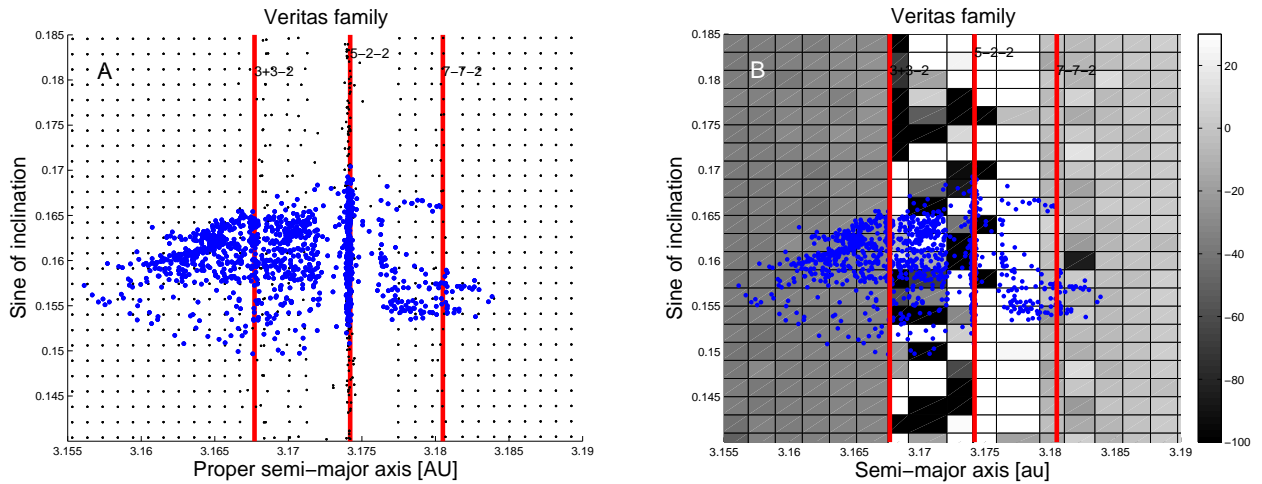


Figure 19. An $(a, \sin i)$ dynamical map of the region of the Veritas family (Panel A). Black dots identify the values of synthetic proper elements of the integrated test particles. Other symbols are the same as in Fig. 1. Panel B displays a colour plot of values of $\delta s/\delta a$ obtained for the particles in the dynamical map simulation.

the role of the local dynamics, we first obtained a dynamical map of synthetic proper elements in the $(a, \sin i)$ domain.

For this purpose, we created a grid of 1600 particles divided in 40 equally spaced intervals in both osculating a and i and integrated them over 12 Myr over the influence of the sun and the eight planets with *SWIFT_MVSEF*, the symplectic integrator based on *SWIFT_MVS* from the *Swift* package of [Levison & Duncan \(1994\)](#), and modified by [Brož \(1999\)](#) to include online filtering of osculating elements. The initial osculating elements of the particles went from 3.150 to 3.190 au in a and from 7.0° to 11.0° in i . The other orbital elements of the test particles were set equal to those of (1086) *Nata* at the modified Julian date of 57200. The step in osculating a , 0.001 au, was chosen small enough to allow for a significant resolution in the map, but large enough so that the computation of $\delta s/\delta a$ and $\delta g/\delta a$ was precise enough, considering the errors in proper frequencies and semi-major axis. Synthetic proper elements were then obtained with the

approach described in [Carruba \(2010\)](#), based on the method of [Knežević and Milani \(2003\)](#).

Results are shown in Fig. 19, panel A. Black dots display the location of the test particles synthetic proper elements. Not surprisingly, one can notice i) the important perturbing effect of the 5-2-2 resonance, and ii) the absence of important secular resonances in this region, apart from the $\nu_{1H} = g - g_{Hygiea}$ located at $\simeq 3.170$ au (not shown in the figure for simplicity), that further contributes to the chaotic dynamics between the 3+3-2 and 5-2-2 three-body resonances. Based on the values of proper frequencies g and s obtained for this map, we then computed the values of $\delta g/\delta a$ and $\delta s/\delta a$ with this method: for each point in the line of 40 intervals in a in the map, with the exception of the first and last, we computed the distance in proper a , da , and in proper frequencies dg and ds of the neighbor to the left with respect to the neighbor to the right. $\delta g/\delta a$ and $\delta s/\delta a$ were then assumed equal to dg/da and ds/da , respectively. Results are

shown in Fig. 19, panel B, display a color plot of our results for $\delta s/\delta a$ (results for $\delta g/\delta a$ are analogous and will not be shown, for simplicity). For semi-major axis lower than those of the center of the 3+3-2 resonance the behavior of $\delta s/\delta a$ is quite regular, slowly increasing with respect to a . $\delta s/\delta a$ becomes much more erratic between the 3+3-2 and 5-2-2 resonances, and only returns to a more regular behavior for values of semi-major axis larger than 3.18 au, beyond the locations of the 5-2-2 and the 7-7-2 three-body resonances. In view of the complex behavior observed for $\delta s/\delta a$ and $\delta g/\delta a$, we decided not to use an analytic approach to obtain family ages and drift rates based on these values.

11 APPENDIX 2: YARKOVSKY DRIFT SPEED VALUES

We report in Table 1 the first 10 identified Veritas members, their absolute magnitude, proper $a, e, \sin i, g$, and s , Lyapunov exponent (multiplied by a factor 10^6), and estimated mean Yarkovsky drift speed, in au/Myr (no such value is available for (1086) *Nata* itself, that because of its relative large size has very limited Yarkovsky mobility).

Table 1: Proper elements and estimated drift rates of 274 Veritas family members.

Number	H	a_P [au]	e_P	$\sin i_P$	g_P ["/yr]	s_P ["/yr]	$LCE * 10^6$ [yr $^{-1}$]	Drift speed [au/Myr]
1086	9.49	3.165357	0.061441	0.161970	127.944574	-81.597922	1.45	0.000E+00
6374	11.95	3.165615	0.061238	0.161059	128.412635	-81.663237	1.34	-0.800E-04
7231	12.14	3.165802	0.061364	0.160469	128.750656	-81.730850	0.33	-0.220E-03
8624	13.55	3.164742	0.061074	0.162768	127.137085	-81.472127	1.47	0.800E-03
9715	13.23	3.165485	0.060828	0.159609	128.625973	-81.736346	1.87	-0.740E-03
9860	13.07	3.164893	0.060683	0.161880	127.484952	-81.514396	1.46	-0.140E-03
11768	12.93	3.164016	0.060272	0.162164	126.564674	-81.416291	1.50	0.300E-03
15066	12.23	3.165616	0.061469	0.162364	128.100351	-81.579624	1.38	-0.240E-03
15256	12.52	3.164626	0.060472	0.161926	127.209465	-81.479886	1.52	0.820E-03
15732	12.38	3.164794	0.060991	0.162029	127.366566	-81.526495	1.40	0.999E-04
17439	13.80	3.162809	0.059831	0.160005	125.957459	-81.496475	1.70	0.200E-04
17701	12.44	3.165318	0.061097	0.162130	127.851683	-81.550972	1.49	0.300E-02
18476	13.30	3.164524	0.060754	0.162374	127.014041	-81.465351	1.44	-0.800E-04
25828	13.02	3.164705	0.060953	0.161937	127.303391	-81.526761	1.48	-0.180E-03
28546	12.35	3.165455	0.061326	0.163226	127.722333	-81.489204	1.54	0.680E-03
28908	13.10	3.164650	0.060736	0.162437	127.117559	-81.464060	1.45	0.000E+00
31743	12.59	3.164265	0.060567	0.161117	127.071091	-81.538253	1.50	0.500E-03
35041	14.81	3.164042	0.060291	0.159507	127.244037	-81.632330	1.51	-0.400E-03
37360	13.57	3.161214	0.058530	0.158279	124.892780	-81.447510	1.47	0.300E-03
38419	13.84	3.163684	0.059980	0.160858	126.564888	-81.480149	1.47	-0.580E-03
42776	12.84	3.164625	0.060862	0.161532	127.324448	-81.547888	1.48	0.120E-03
45727	13.41	3.163868	0.060452	0.160952	126.732618	-81.523407	0.36	0.180E-03
46350	13.79	3.164370	0.060277	0.163091	126.669979	-81.356635	1.45	0.160E-03
46412	14.05	3.163083	0.059002	0.160831	125.973686	-81.367718	1.59	0.720E-03
47641	14.22	3.161093	0.058860	0.159794	124.435418	-81.350636	1.09	0.000E+00
50182	13.04	3.164896	0.061141	0.162245	127.419207	-81.527880	1.44	-0.120E-03
51336	13.01	3.163305	0.059763	0.160663	126.253041	-81.459604	1.35	-0.660E-03
52551	13.62	3.164611	0.060742	0.162598	127.042241	-81.449701	1.55	0.000E+00
54354	13.86	3.165539	0.061478	0.161905	128.141623	-81.614246	1.49	0.460E-03
54592	13.89	3.164968	0.061088	0.161707	127.620458	-81.569666	1.53	-0.220E-03
57012	14.03	3.164837	0.060983	0.162208	127.365196	-81.513115	1.33	0.800E-04
57753	14.44	3.164231	0.060510	0.162583	126.675971	-81.413634	1.47	0.440E-03
57950	14.05	3.161606	0.059459	0.158770	125.160602	-81.508210	0.18	0.520E-03
60256	14.01	3.164504	0.060246	0.161217	127.260845	-81.511176	1.48	-0.120E-03
60329	13.96	3.163761	0.060284	0.160477	126.744086	-81.541785	1.68	0.140E-03
60605	13.59	3.164496	0.060418	0.163034	126.810078	-81.379503	1.54	0.600E-03
62467	13.92	3.162568	0.059634	0.159219	125.922575	-81.531169	0.28	-0.340E-03
72563	13.78	3.164477	0.060664	0.160876	127.337461	-81.576150	1.52	0.999E-04
72819	14.13	3.164171	0.060300	0.159489	127.371670	-81.640429	1.60	0.860E-03
78726	14.55	3.164401	0.060356	0.163143	126.690025	-81.360469	1.49	0.540E-03
81935	13.61	3.164941	0.061000	0.162855	127.306185	-81.467112	1.49	-0.440E-03
82961	13.97	3.163596	0.059972	0.160924	126.467789	-81.470525	1.56	0.220E-03
83253	14.21	3.164422	0.060193	0.157813	128.014094	-81.774563	1.74	-0.300E-03
83802	14.38	3.161932	0.059400	0.160545	125.018547	-81.375745	1.28	0.580E-03
86285	13.71	3.165185	0.060962	0.161573	127.858357	-81.577812	1.50	-0.340E-03
87898	14.37	3.164912	0.060382	0.162060	127.448558	-81.473145	0.04	-0.460E-03
90252	14.64	3.162968	0.059721	0.159632	126.192638	-81.523771	1.25	-0.400E-03
91850	14.51	3.160705	0.058510	0.159686	124.110854	-81.311467	1.63	0.620E-03
92131	14.20	3.163030	0.059763	0.158249	126.586142	-81.640068	1.39	-0.779E-03
94167	14.48	3.162193	0.059465	0.160524	125.260672	-81.395188	1.56	-0.580E-03
94285	14.13	3.165299	0.061409	0.162704	127.707209	-81.532720	1.49	0.122E-02
95505	14.72	3.160562	0.058394	0.154249	125.270716	-81.720492	1.27	0.600E-03
96549	14.34	3.163247	0.059840	0.158451	126.740241	-81.640343	1.42	-0.180E-03
97654	13.94	3.163692	0.060497	0.161069	126.544221	-81.510822	1.74	0.740E-03
105854	13.98	3.164814	0.061434	0.161874	127.447695	-81.581781	1.47	0.420E-03
106551	14.44	3.157830	0.055532	0.155412	122.585895	-81.262210	1.36	-0.220E-03

Continued on next page

Table 1 – Continued from previous page

Number	H	a_P [au]	e_P	$\sin i_P$	g_P ["/yr]	s_P ["/yr]	$LCE * 10^6$ [yr $^{-1}$]	Drift speed [au/Myr]
110595	14.38	3.162904	0.057505	0.150796	128.140527	-82.010671	1.44	-0.940E-03
111713	14.74	3.164573	0.060242	0.162772	126.940836	-81.387432	1.44	-0.180E-03
112107	14.40	3.163064	0.059862	0.160615	126.047631	-81.462291	1.40	0.200E-03
113283	14.07	3.164308	0.060750	0.162749	126.719298	-81.425637	1.20	0.000E+00
115211	14.00	3.164560	0.060443	0.162713	126.952903	-81.410589	1.47	0.200E-04
127336	14.21	3.161449	0.059159	0.160294	124.640439	-81.352844	0.51	0.280E-03
129117	14.86	3.157537	0.055855	0.155113	122.429214	-81.298008	0.43	0.200E-03
130355	14.91	3.165214	0.060437	0.158157	128.702083	-81.803724	1.41	-0.620E-03
130360	14.66	3.164541	0.060989	0.162446	127.024392	-81.482036	0.50	0.400E-04
132750	13.73	3.165298	0.061292	0.161462	128.009493	-81.622310	1.50	0.000E+00
132849	14.25	3.164530	0.060361	0.159409	127.734302	-81.667893	1.49	-0.200E-04
132861	14.29	3.164179	0.060180	0.161037	126.994440	-81.505254	1.38	0.200E-04
135404	14.42	3.164697	0.060773	0.161383	127.427027	-81.554788	1.19	0.000E+00
135416	14.49	3.160482	0.058240	0.159432	123.966463	-81.298099	1.55	-0.520E-03
138569	14.80	3.163351	0.059506	0.160743	126.264671	-81.432080	1.52	0.220E-03
138747	14.51	3.165347	0.060746	0.159569	128.499718	-81.725999	1.44	0.240E-03
138758	14.38	3.165422	0.061351	0.161845	128.036724	-81.601904	1.41	0.108E-02
141189	14.62	3.163511	0.060015	0.160236	126.557860	-81.525640	1.79	0.420E-03
144405	14.62	3.165479	0.061113	0.162716	127.865280	-81.511759	0.00	-0.580E-03
145894	14.66	3.165646	0.061088	0.161916	128.226823	-81.581238	1.51	0.700E-03
147948	14.90	3.164483	0.060393	0.162742	126.868661	-81.399981	1.48	-0.120E-03
149141	14.78	3.161778	0.059075	0.160083	124.979202	-81.376913	1.25	0.800E-04
150320	14.01	3.164077	0.060115	0.161041	126.894299	-81.494536	1.43	-0.779E-03
153169	14.61	3.163763	0.060351	0.162197	126.326428	-81.410094	1.58	-0.400E-04
155231	15.00	3.163095	0.059924	0.159959	126.237566	-81.521071	0.87	-0.160E-03
155463	14.70	3.164984	0.061019	0.162578	127.416392	-81.492734	1.47	0.600E-04
157463	14.52	3.163610	0.059855	0.160753	126.516740	-81.474283	1.48	0.999E-04
162156	14.84	3.165859	0.061219	0.164015	127.915770	-81.431502	1.45	0.150E-02
168041	15.17	3.164292	0.060234	0.162945	126.630872	-81.361212	1.49	-0.520E-03
169282	14.50	3.164507	0.060058	0.162416	126.957856	-81.396788	1.49	0.600E-04
169314	14.81	3.162605	0.059784	0.160395	125.677826	-81.452821	1.14	0.116E-02
169398	14.75	3.164175	0.060304	0.159836	127.290531	-81.613062	1.51	0.999E-04
176576	14.63	3.164367	0.060320	0.160172	127.389730	-81.595561	1.50	-0.560E-03
178745	14.59	3.162774	0.059407	0.160669	125.747721	-81.403791	1.28	0.000E+00
179448	14.66	3.164581	0.060632	0.162481	127.036884	-81.447747	1.15	0.400E-04
181265	15.69	3.162109	0.057693	0.163171	124.465833	-81.022891	1.47	0.620E-03
181598	15.19	3.163722	0.058446	0.152527	128.536483	-81.997301	1.53	0.500E-03
186634	15.01	3.164985	0.060455	0.161774	127.590964	-81.506008	1.49	-0.800E-04
188944	14.87	3.163005	0.059501	0.162372	125.545823	-81.285939	1.79	-0.999E-04
191443	14.43	3.162569	0.059473	0.160662	125.565330	-81.401444	0.26	0.680E-03
192460	15.03	3.163392	0.059904	0.160924	126.274037	-81.455694	1.51	0.999E-04
192604	15.48	3.165851	0.060891	0.159678	128.972717	-81.752176	1.52	0.120E-02
196134	14.79	3.165773	0.060646	0.157670	129.377797	-81.886030	1.50	-0.800E-04
197076	15.21	3.164561	0.060107	0.163156	126.826630	-81.343886	1.32	-0.400E-04
198745	14.86	3.165625	0.060803	0.158543	129.023528	-81.824357	1.28	-0.220E-03
200365	14.88	3.161320	0.058877	0.159895	124.609717	-81.353918	1.24	0.400E-04
202319	15.11	3.163660	0.059915	0.162666	126.092772	-81.327007	0.95	0.560E-03
207576	15.54	3.164195	0.060311	0.159170	127.471084	-81.667825	1.41	-0.140E-03
208453	14.87	3.165235	0.061341	0.160429	128.203393	-81.707337	1.38	0.380E-03
209410	15.23	3.158645	0.056316	0.156275	123.082688	-81.297274	0.48	0.900E-03
210067	15.40	3.164961	0.060973	0.160719	127.850600	-81.637836	1.43	0.258E-02
210171	15.32	3.161992	0.059545	0.158566	125.554539	-81.549477	1.48	0.620E-03
210431	15.13	3.165053	0.060528	0.158316	128.509419	-81.792582	1.49	0.300E-03
214439	15.84	3.164329	0.060334	0.161223	127.094467	-81.510907	1.62	-0.380E-03
214560	15.59	3.164763	0.061019	0.162386	127.250341	-81.499325	1.51	-0.180E-03
215011	15.77	3.165512	0.059723	0.164306	127.435501	-81.255152	1.79	-0.400E-04
216775	14.85	3.165294	0.061470	0.162832	127.670473	-81.527715	1.58	0.274E-02
217140	15.24	3.165071	0.060921	0.162636	127.478097	-81.482940	1.65	0.460E-03

Continued on next page

Table 1 – *Continued from previous page*

Number	H	a_P [au]	e_P	$\sin i_P$	g_P ["/yr]	s_P ["/yr]	$LCE * 10^6$ [yr ⁻¹]	Drift speed [au/Myr]
217391	15.13	3.164550	0.060301	0.159361	127.759919	-81.666721	0.00	-0.360E-03
220777	14.44	3.164048	0.059943	0.161029	126.859958	-81.478476	1.41	0.000E+00
223398	15.91	3.160882	0.058613	0.159697	124.262112	-81.327265	0.83	0.400E-04
223862	15.22	3.161153	0.058558	0.158288	124.836266	-81.445759	1.29	0.000E+00
225150	15.50	3.164971	0.060411	0.161581	127.621764	-81.516916	1.48	-0.800E-03
226517	14.81	3.165446	0.060499	0.163492	127.608311	-81.389947	1.46	-0.340E-03
232975	15.04	3.165695	0.061124	0.160842	128.539577	-81.673463	0.38	0.180E-03
233908	14.84	3.165270	0.060492	0.163719	127.380312	-81.362877	1.48	0.108E-02
234440	15.56	3.163900	0.059546	0.160984	126.715039	-81.439944	1.34	-0.500E-03
236668	16.14	3.163575	0.059868	0.162278	126.106596	-81.350946	1.49	-0.580E-03
236811	15.51	3.158787	0.057676	0.155852	123.351490	-81.452657	1.47	0.000E+00
236970	14.72	3.163826	0.060369	0.160669	126.757684	-81.536676	1.38	0.460E-03
237363	15.44	3.160700	0.057110	0.153021	125.623586	-81.708655	1.49	0.400E-04
238392	15.72	3.163708	0.060423	0.161094	126.545628	-81.502554	1.49	0.999E-04
238402	15.74	3.164935	0.061329	0.160998	127.771335	-81.647583	1.49	0.360E-03
239217	15.44	3.164584	0.059879	0.162759	126.935285	-81.355890	1.74	-0.200E-03
240266	15.07	3.165718	0.061261	0.163636	127.870964	-81.460219	1.72	0.460E-03
240533	15.26	3.165634	0.061105	0.159050	128.921164	-81.812696	1.34	-0.800E-04
241998	15.14	3.162766	0.059713	0.157700	126.469989	-81.666927	1.55	-0.600E-04
242017	15.50	3.161123	0.057848	0.153468	125.920053	-81.757651	1.37	0.800E-04
242288	14.98	3.164966	0.060766	0.158795	128.317605	-81.772948	1.48	0.400E-03
242675	15.36	3.162021	0.059653	0.159677	125.316910	-81.471837	0.75	0.126E-02
242959	15.09	3.165335	0.061364	0.163139	127.626949	-81.494192	1.52	0.000E+00
244159	15.30	3.163505	0.059877	0.159672	126.680950	-81.557847	1.61	-0.940E-03
245064	15.88	3.165459	0.066143	0.162188	128.211747	-82.045206	1.24	-0.140E-03
245488	15.55	3.164897	0.060454	0.161478	127.577404	-81.525969	1.58	-0.700E-03
245494	14.87	3.164868	0.059949	0.163625	126.994682	-81.304405	1.50	0.280E-03
246756	16.21	3.163959	0.058865	0.153337	128.585278	-81.983080	1.43	-0.140E-03
248121	15.31	3.164166	0.059996	0.161251	126.918623	-81.471037	1.56	0.360E-03
249273	16.00	3.163570	0.058890	0.163030	125.874804	-81.201645	1.19	-0.112E-02
249492	15.50	3.162780	0.059558	0.158085	126.383466	-81.622981	1.69	0.400E-04
250082	15.28	3.163844	0.060025	0.163399	126.086687	-81.285654	1.54	0.720E-03
251802	16.00	3.165060	0.060615	0.158457	128.483955	-81.789748	1.48	0.999E-04
251842	15.89	3.164093	0.060188	0.157388	127.800984	-81.793108	0.38	0.000E+00
252834	15.41	3.161034	0.058779	0.159778	124.382255	-81.342040	0.00	0.999E-04
254391	15.52	3.162598	0.059654	0.160165	125.719198	-81.458722	1.89	0.400E-04
255243	14.98	3.163279	0.060096	0.160718	126.226480	-81.484260	1.49	-0.360E-03
255332	14.97	3.163638	0.060332	0.159539	126.857059	-81.616191	0.28	0.800E-04
257098	15.21	3.164292	0.060765	0.161463	127.018818	-81.529931	1.45	0.779E-03
258829	15.21	3.163789	0.060245	0.158904	127.149357	-81.665102	1.50	0.820E-03
261446	15.94	3.165503	0.060245	0.161783	128.078475	-81.507648	1.73	-0.132E-02
261464	15.70	3.162839	0.060209	0.159711	126.072233	-81.556055	1.53	0.000E+00
261618	15.39	3.162828	0.059794	0.158380	126.367283	-81.623442	1.49	-0.540E-03
261709	14.83	3.161433	0.059111	0.160159	124.653800	-81.359114	1.42	0.440E-03
263510	15.80	3.162995	0.059260	0.157257	126.767162	-81.670741	1.49	-0.600E-03
264821	14.91	3.164648	0.060329	0.161236	127.393036	-81.522619	1.47	-0.220E-03
265059	15.79	3.165989	0.060934	0.163733	128.099557	-81.433257	0.43	-0.720E-03
265082	14.95	3.161647	0.058775	0.159106	125.084788	-81.422318	0.00	0.999E-04
265109	15.04	3.165357	0.061343	0.162340	127.847634	-81.558692	1.37	0.112E-02
265446	14.99	3.163480	0.060108	0.160053	126.575615	-81.547300	1.39	-0.560E-03
268202	15.69	3.158716	0.057002	0.159210	122.474700	-81.129063	1.19	0.000E+00
268204	16.16	3.164260	0.060228	0.158899	127.593441	-81.684279	1.53	0.000E+00
269924	15.58	3.162917	0.059756	0.160118	126.024947	-81.485324	0.31	0.640E-03
270913	15.56	3.162643	0.059205	0.162654	125.132029	-81.220354	1.47	-0.520E-03
271223	16.48	3.162183	0.059181	0.155955	126.335455	-81.730302	0.00	0.108E-02
272045	15.41	3.164130	0.059526	0.161240	126.867470	-81.427413	1.53	0.400E-04
272073	15.55	3.165127	0.059809	0.164110	127.114848	-81.262976	1.42	0.360E-03
274064	15.43	3.164794	0.060375	0.161382	127.499445	-81.522054	1.48	-0.580E-03

Continued on next page

Table 1 – Continued from previous page

Number	H	a_P [au]	e_P	$\sin i_P$	g_P ["/yr]	s_P ["/yr]	$LCE * 10^6$ [yr $^{-1}$]	Drift speed [au/Myr]
274752	15.48	3.165504	0.061692	0.161935	128.107137	-81.630518	1.06	0.120E-03
275175	15.60	3.161495	0.059023	0.159929	124.761600	-81.372206	0.79	-0.280E-03
276667	15.55	3.163017	0.058711	0.161325	125.778854	-81.299834	1.77	-0.480E-03
279094	14.73	3.164100	0.059880	0.162286	126.595862	-81.373552	1.30	0.999E-04
279368	15.55	3.165825	0.059627	0.154176	130.227072	-82.067778	1.55	-0.120E-03
279436	15.19	3.162593	0.059216	0.160613	125.587276	-81.383384	0.94	0.880E-03
279499	16.41	3.165116	0.060281	0.156714	128.947909	-81.899027	1.63	0.420E-03
280167	15.30	3.163826	0.060624	0.161277	126.619650	-81.511388	1.53	0.600E-03
281319	15.36	3.162761	0.059511	0.159742	125.964370	-81.486635	1.68	0.160E-03
282384	14.94	3.163622	0.059753	0.157618	127.282963	-81.714616	1.36	0.600E-03
283206	15.54	3.163475	0.060202	0.160776	126.397973	-81.498000	1.53	0.200E-03
284839	15.29	3.163418	0.059624	0.160720	126.337973	-81.447818	1.07	-0.400E-03
284916	15.65	3.163443	0.060171	0.160625	126.403503	-81.505721	1.56	0.118E-02
285109	14.87	3.164236	0.060586	0.163234	126.518840	-81.367510	1.81	0.128E-02
285135	15.64	3.163752	0.059850	0.160395	126.733851	-81.508312	1.29	-0.740E-03
290614	16.16	3.164968	0.060752	0.161216	127.724092	-81.577593	1.55	-0.200E-03
290828	16.49	3.164837	0.060467	0.163868	126.925442	-81.330094	1.54	0.142E-02
292125	15.93	3.164360	0.059792	0.162810	126.706765	-81.334231	1.49	0.580E-03
292308	15.53	3.165903	0.061318	0.161773	128.521575	-81.625243	1.41	-0.460E-03
294550	15.55	3.162395	0.059787	0.157771	126.118251	-81.651333	1.55	0.184E-02
294595	15.49	3.164692	0.060991	0.162565	127.135632	-81.478886	1.75	0.340E-03
294648	15.60	3.165151	0.060691	0.162596	127.555129	-81.468502	1.52	-0.142E-02
294679	15.88	3.162807	0.059461	0.158989	126.186503	-81.543748	1.58	-0.300E-03
295434	16.32	3.165106	0.060814	0.162282	127.595498	-81.503171	1.52	-0.480E-03
296630	15.65	3.163898	0.059894	0.161000	126.724389	-81.470412	1.23	0.400E-04
296907	15.15	3.162259	0.059159	0.162486	124.825102	-81.212471	1.51	0.260E-03
296992	15.97	3.163334	0.059873	0.162633	125.796713	-81.311911	1.25	0.800E-03
299255	16.00	3.163117	0.059725	0.160711	126.063377	-81.443809	1.51	0.640E-03
299298	15.29	3.161891	0.059605	0.157875	125.632031	-81.604579	1.48	0.880E-03
299320	16.04	3.165256	0.061116	0.159802	128.368339	-81.737822	1.62	0.700E-03
300116	15.63	3.162525	0.058826	0.158902	125.923633	-81.481553	0.24	-0.580E-03
300181	16.09	3.161305	0.057411	0.160545	124.380538	-81.173678	0.69	0.400E-04
300195	15.00	3.161911	0.058860	0.161893	124.647411	-81.218865	0.00	0.920E-03
300866	15.06	3.163028	0.059724	0.158290	126.568884	-81.632876	0.00	-0.640E-03
300909	15.36	3.161764	0.059116	0.162675	124.334935	-81.172024	1.49	0.779E-03
303795	16.19	3.159267	0.057610	0.159627	122.857829	-81.172798	2.00	-0.640E-03
306092	16.06	3.165384	0.060745	0.162211	127.878895	-81.514098	1.56	-0.102E-02
306983	15.30	3.165449	0.060594	0.157721	129.042951	-81.863350	1.14	0.340E-03
308390	15.59	3.158472	0.057217	0.159333	122.252852	-81.126933	0.00	-0.440E-03
308419	15.27	3.164179	0.060792	0.162802	126.582147	-81.418880	1.45	0.440E-03
308493	16.16	3.165524	0.061208	0.160170	128.542529	-81.727987	1.50	0.204E-02
315842	15.68	3.157401	0.055411	0.155736	122.155088	-81.206610	1.57	0.300E-03
316525	15.49	3.164097	0.060834	0.162869	126.490692	-81.414344	1.73	0.800E-03
318349	15.66	3.164527	0.064169	0.151597	129.786494	-82.649432	1.40	-0.800E-04
319165	15.66	3.165422	0.061074	0.162303	127.907391	-81.538572	1.42	-0.440E-03
320061	15.74	3.165483	0.061365	0.164066	127.539477	-81.425153	0.35	0.600E-03
322203	15.83	3.165699	0.058617	0.150899	130.837567	-82.222504	1.92	0.240E-02
323274	15.74	3.163064	0.059469	0.161069	125.915541	-81.389830	1.47	0.800E-03
324281	15.99	3.164318	0.060670	0.162564	126.767537	-81.433510	1.66	0.300E-03
324754	16.09	3.164700	0.060102	0.161305	127.416795	-81.499257	1.30	-0.460E-03
325369	15.45	3.165509	0.060856	0.158733	128.865128	-81.809477	1.52	-0.600E-04
326258	15.22	3.165193	0.060897	0.161913	127.774356	-81.544110	1.49	-0.600E-03
328045	16.19	3.165402	0.061389	0.163612	127.575281	-81.461305	1.42	0.246E-02
333826	15.83	3.163153	0.059920	0.159504	126.398803	-81.559812	1.41	0.800E-04
336481	15.88	3.164781	0.060901	0.162270	127.290717	-81.498596	1.42	-0.146E-02
340685	15.38	3.164659	0.063509	0.161752	127.421121	-81.782518	1.69	-0.620E-03
341786	15.31	3.165139	0.061075	0.163770	127.267399	-81.407801	0.61	0.180E-02
343046	15.65	3.164041	0.060351	0.161012	126.875341	-81.516932	1.50	-0.140E-03

Continued on next page

Table 1 – *Continued from previous page*

Number	H	a_P [au]	e_P	$\sin i_P$	g_P ["/yr]	s_P ["/yr]	$LCE * 10^6$ [yr ⁻¹]	Drift speed [au/Myr]
343049	15.59	3.162848	0.059614	0.158463	126.358237	-81.601377	1.54	-0.700E-03
343575	16.32	3.165058	0.059381	0.164406	126.955566	-81.196880	1.52	-0.500E-03
343595	15.44	3.157092	0.055573	0.155409	121.988603	-81.231548	1.54	0.600E-04
344374	15.36	3.163667	0.059935	0.162254	126.201344	-81.362347	1.45	0.112E-02
345648	15.98	3.162758	0.059920	0.162310	125.351615	-81.317593	1.14	0.660E-03
346796	16.33	3.165287	0.058259	0.151276	130.326147	-82.143604	1.19	-0.660E-03
346835	15.88	3.164113	0.060119	0.158943	127.439879	-81.664048	1.57	0.200E-04
349308	15.61	3.164205	0.059705	0.160838	127.045273	-81.479340	1.71	-0.800E-03
350123	16.57	3.165857	0.061487	0.159867	128.958052	-81.793218	1.44	-0.260E-03
350804	16.29	3.163354	0.058801	0.153874	127.889029	-81.909963	1.45	-0.160E-03
351936	16.35	3.164296	0.060155	0.161315	127.032968	-81.485795	1.45	-0.380E-03
351967	15.50	3.160332	0.057891	0.159704	123.756953	-81.239161	0.57	0.300E-03
352544	15.93	3.162226	0.058204	0.160637	125.209410	-81.275902	0.36	-0.560E-03
354702	16.21	3.161734	0.059102	0.162556	124.337648	-81.179040	1.71	0.300E-03
355679	15.34	3.164887	0.060638	0.163388	127.101979	-81.387406	1.45	0.600E-03
356365	15.79	3.163559	0.060594	0.160053	126.670234	-81.595212	1.79	0.560E-03
360117	15.60	3.163673	0.059720	0.160923	126.526762	-81.450891	1.44	0.440E-03
361491	15.66	3.159413	0.058016	0.157061	123.606657	-81.416280	0.13	0.300E-03
362477	15.88	3.165544	0.060626	0.157818	129.114604	-81.862845	1.55	0.480E-03
362566	15.51	3.162657	0.059276	0.160484	125.679785	-81.401422	1.46	0.140E-03
363484	15.44	3.164353	0.059763	0.162674	126.734586	-81.342618	1.48	-0.520E-03
363869	15.88	3.162682	0.059973	0.162599	125.214211	-81.295715	1.23	0.204E-02
364562	16.17	3.165703	0.060025	0.163580	127.815399	-81.349777	0.19	-0.136E-02
365379	15.85	3.163508	0.058330	0.154015	127.978952	-81.862631	1.25	-0.880E-03
365514	15.73	3.161317	0.058618	0.159061	124.798319	-81.397986	0.58	0.116E-02
365809	15.82	3.163723	0.060165	0.161034	126.564824	-81.484545	1.27	0.900E-03
366523	16.16	3.159244	0.056049	0.154123	124.076467	-81.467856	0.00	-0.520E-03
366544	16.45	3.162277	0.057536	0.151725	127.349253	-81.914754	1.43	-0.200E-03
366804	16.19	3.165315	0.061056	0.160385	128.279357	-81.687629	1.50	-0.420E-03
368082	15.90	3.163981	0.059517	0.161034	126.777784	-81.436465	0.37	0.120E-03
369180	16.24	3.164120	0.060602	0.161870	126.750064	-81.474264	1.44	0.500E-03
370407	16.14	3.161200	0.059732	0.159108	124.729105	-81.487202	1.87	0.840E-03
373385	15.10	3.164062	0.060718	0.161308	126.839681	-81.528174	1.51	0.520E-03
373392	15.91	3.156675	0.055445	0.156193	121.470180	-81.141158	1.65	0.340E-03
379091	15.93	3.164728	0.061350	0.161280	127.506180	-81.618046	1.49	0.380E-03
384154	16.04	3.160966	0.056247	0.159521	124.286864	-81.141267	1.66	0.200E-04
386237	15.90	3.164115	0.060201	0.158957	127.442750	-81.671175	1.49	0.180E-03
386253	16.15	3.164490	0.060548	0.163292	126.745194	-81.369909	1.48	0.860E-03
388363	15.58	3.164903	0.060665	0.163347	127.129947	-81.394252	1.44	0.740E-03
389221	16.49	3.165599	0.065974	0.162128	128.358144	-82.038951	1.48	0.779E-03
390971	16.14	3.159913	0.058079	0.155569	124.386518	-81.560901	1.63	0.640E-03
391728	16.06	3.165533	0.066185	0.162052	128.322252	-82.063738	1.47	-0.300E-03
392556	16.31	3.163863	0.065132	0.155402	128.294777	-82.417095	1.73	-0.264E-02
392580	16.05	3.162223	0.057426	0.160864	125.120510	-81.189675	1.75	-0.110E-02

REFERENCES

- Bendjoya, P., Zappalà, V. 2002, in Asteroid III (W. Bottke, A. Cellino, P. Paolicchi, R. Binzel Eds.), Univ. Arizona Press, 613.
- Bottke, W. F., Nolan, M. C., Kolvoord, R. A., Greenberg, R., 1994, *Icarus*, 107, 255.
- Bottke, W. F., Vokrouhlický, D., Rubincam, D.P., Brož, M. 2002, in Asteroid III (W. Bottke, A. Cellino, P. Paolicchi, R. Binzel Eds.), Univ. Arizona Press, 395.
- Bottke, W. F., Vokrouhlický, D., Rubincam, D. P., Nesvorný, D., 2006, *Annu. Rev. Earth Planet. Sci.*, 34, 157.
- Brož, M., Thesis, Charles Univ., Prague, Czech Republic.
- Brož, M., Morbidelli, A., Bottke, W. F., Rozehnal, J., Vokrouhlický, D., Nesvorný, D. 2013, *A&A* 551, A117.
- Carruba, V., Burns, J. A., Bottke, W., Nesvorný, D., 2003, *Icarus*, 162, 308.
- Carruba, V. 2010, *MNRAS*, 408, 580.
- Carruba, V., Huaman, M., Douwens, S., & Domingos, R. C. 2012, *A&A*, 543, A105.
- Carruba, V., Huaman, M., Domingos, R. C., Roig, F., 2013. *A&A* 550, A85.
- Carruba, V., 2013. *MNRAS*, 431, 3557.
- Carruba, V., Domingos, R. C., Huaman, M., Dos Santos, C. R., Souami, D., 2014, *MNRAS*, 437, 2279.
- Carruba, V., Nesvorný, D., 2016, *MNRAS*, 457, 1332.
- Carruba, V., Nesvorný, D., Vokrouhlický, D. 2016, *AJ*, 151, 164.
- Delbò, M., Mueller, M., Emery, J. P., Rozitis, B., Capria, M. T., 2015, in Asteroids IV, (P. Michel, F. E. DeMeo, W. Bottke Eds.), Univ. Arizona Press, 107.
- DeMeo, F. E., Carry, B., 2013, *Icarus*, 226, 723.
- Farley, K. A., Vokrouhlický, D., Bottke, W. F., & Nesvorný, D. 2006, *Nature*, 439, 295.
- Ivezić, Ž, and 34 co-authors, 2001, *AJ*, 122, 2749.
- Knežević, Z., Milani, A., 2003, *A&A*, 403, 1165.
- Levison, H. F., Duncan, M. J., 1994, *Icarus*, 108, 18.
- Masiero, J. R., Mainzer, A. K., Grav, T., Bauer, J. M., and Jedicke, R., 2012, *ApJ*, 759, 14.
- Michel, P., Jutzi, M., Richardson, D. C., Benz, W., 2011, *Icarus*, 211, 535.
- Migliorini, F. Nesvorný, D., Zappalà, V., 1988, *Science*, 281, 2022.
- Milani, A., & Farinella, P. 1994, *Nature*, 370, 40.
- Milani, A., Knežević, Z., 1994, *Icarus*, 107, 219.
- Murray, C. D., Dermott, S. F. 1999. *Solar system dynamics*. Cambridge University Press, 1999.
- Nesvorný, D., Bottke, W. F., Jr., Dones, L., Levison, H. F. 2002. *Nature* 417, 720.
- Nesvorný, D., Bottke, W. F., Levison, H. F., Dones, L. 2003, *AJ*, 591, 486.
- Nesvorný, D., Bottke, W. F., 2004, *Icarus*, 170, 324.
- Nesvorný, D., Brož, M., Carruba, V. 2015, In Asteroid IV, (P. Michel, F. E. DeMeo, W. Bottke Eds.), Univ. Arizona Press, 297.
- Pravec, P., Harris, A. W., Michalowski, T., 2002, in Asteroids III, (W. Bottke, A. Cellino, P. Paolicchi, R. Binzel Eds.), Univ. Arizona Press, 113.
- Scheeres, D. J., Britt, D., Carry, B., Holsapple, K. A., 2015, in Asteroids IV, (P. Michel, F. E. DeMeo, W. Bottke Eds.), Univ. Arizona Press, 745.
- Tsiganis, K., Knežević, Z., Varvoglis, H., 2007, *Icarus*, 186, 484.
- Vokrouhlický, D. 1999, *A&A* 334, 362.
- Vokrouhlický, D., Bottke, W. F., Chesley, S. R., Scheeres, D. J., Statler, T. S., 2015, in Asteroids IV, (P. Michel, F. E. DeMeo, W. Bottke Eds.), Univ. Arizona Press, 509.

This paper has been typeset from a $\text{\TeX}/\text{\LaTeX}$ file prepared by the author.